This is the peer-reviewed, final accepted version for American Mineralogist, published by the Mineralogical Society of America.
The published version is subject to change. Cite as Authors (Year) Title. American Mineralogist, in press.
DOI: https://doi.org/10.2138/am-2023-9188. http://www.minsocam.org/

REVISION 2

Polysomatic intergrowths between amphiboles and non-classical pyriboles in magnetite: smallest-scale features recording a protracted geological history

YURI TATIANA CAMPO RODRIGUEZ[1,2,*], CRISTIANA L. CIOBANU[1], ASHLEY SLATTERY[3], NIGEL J. COOK[1], MARIA EMILIA SCHUTESKY[2], KATHY EHRIG[1,4], SAMUEL A. KING[1], JIE YAO[1]

[1]School of Chemical Engineering, The University of Adelaide, Adelaide S.A. 5005, Australia

[2]Geosciences Institute, University of Brasília, Brasília DF 70910-900, Brazil

[3]Adelaide Microscopy, The University of Adelaide, Adelaide S.A. 5005, Australia

[4]BHP Olympic Dam, 10 Franklin Street, Adelaide S.A. 5000, Australia

ABSTRACT

Non-classical pyriboles (NCPs) have tetrahedral silicate chains (I_{beam}) of multiplicity higher than single (pyroxene) or double (amphibole) I_{beams} and are known from amphiboles in altered mafic-ultramafic complexes. NCPs, their polysomatic sequences, and inherent chain-width disorder are petrogenetic tools for interpreting igneous and metamorphic processes. Magnetite, a refractory mineral that can trap and preserve NCPs is a major constituent of iron oxide-copper-gold (IOCG) deposits. We undertook a nanoscale study to show that NCPs and amphiboles are hosted within magnetite cores from the Jatobá Ni-bearing IOCG deposit, Carajás district, Brazil. Monoclinic amphiboles and NCPs form polysomatic intergrowths or occur as sparse inclusions along $\{111\}_{magnetite}$. There are two chemical populations of amphiboles: Mg-Fe- and Ca-(Al)-

* Corresponding author. e-mail: yuri.camporodriguez@adelaide.edu.au; ytcampor@unal.edu.co

This is the peer-reviewed, final accepted version for American Mineralogist, published by the Mineralogical Society of America.
The published version is subject to change. Cite as Authors (Year) Title. American Mineralogist, in press.
DOI: https://doi.org/10.2138/am-2023-9188. http://www.minsocam.org/

amphiboles, the latter including Ce-bearing Mg-hornblende and (ferro)tschermakite. The occurrence contains one of the widest ranges of chain silicates ever recorded, from simple intergrowths of single to triple I_{beam} zippers, including pyroxene slabs, to longer NCP polysomes up to 15-I_{beam} chains. Clinojimthompsonite (Cjim) is observed for the first time within magnetite. Although no discrete polysomes could be defined, the NCP-amphibole intergrowths have composition between Mg-Fe amphiboles and Cjim based on I_{beam} averages of 2.5-2.7. Relationships between increase in the number of *C* and *A* cations from amphibole (2-I_{beam}) to n chain silicates (nI_{beam}) are formulated as $nI_{beam} = T(2+n) = C(5+3n) = A(1+n)$, n=integer. Empirical models of crystal structures, validated by STEM simulation, are shown for 4- and 5-I_{beam} chain silicates. Co-crystallization of double- and triple-chain silicate structures with rhythmic intergrowths as larger blocks along *b* is often accompanied by rhythmic Ca-Fe zonation along *a*, supporting primary NCP crystallization via self-patterning during amphibole growth within magnetite in a close-to-equilibrium system. Chain-width disorder is documented from defects including planar faults, derailments, jogs, and swells.

Violations of zipper termination rules indicate primary growth rather than replacement. Amphibole-NCPs inclusions support a multi-stage evolution for Jatobá magnetite. They formed during the first cycle of magnetite growth within a mafic/ultramafic lithology that records syn-shearing events. Subsequent formation of calcic-amphiboles, including Ce-bearing species, indicate IOCG-related fluids at the onset of mineralization. (Ferro)tschermakite formed at ~7.5 kbar during shearing associated with main ore deposition. The multi-stage amphibole-NCPs generations in magnetite revealed by nanoscale study emphasize the interpretive value of magnetite for overprinting events in terranes with protracted geological histories. Analogous NCPs

are likely to be abundant in magnetite from magmatic-hydrothermal deposits hosted by greenstone belts and altered mafic/ultramafic complexes. Likewise, discovery of Ce-rich hornblende provides new avenues to understand the early, alkali-calcic alteration stages of IOCG systems and models for REE incorporation into, and subsequent release from chain silicates.

Keywords: non-classical pyriboles, (Ce-bearing) amphiboles, magnetite, polysomatic sequences, chain-width disorder, Jatobá Ni-IOCG deposit.

INTRODUCTION

One of the most outstanding examples of crystal-structural modularity in silicates is the group of non-classical pyriboles (NCP) (Bozhilov 2013 and references therein). These minerals are structurally related to inosilicates but have tetrahedral silicate chains with multiplicity higher than single (pyroxene) or double (amphibole) chains. The NCPs are also linked to the biopyribole concept that considers smaller structural modules of pyroxene and mica to build any other chain silicate (Thompson 1978). Such building principles, bridging chain and sheet silicates, lie at the heart of polysomatism concepts used to define polysomatic series and order-disordered intergrowths between various members of those series (e.g., Veblen 1991; Hatert et al. 2023 and references therein). The most recent model (Nespolo and Bouznari 2018) unifies biopyribole and palysepiole polysomatic series using a framework of tropochemical cell twinning. The discovery of triple chain silicates, clinojimthompsonite (Cjim) and alternating double and triple chain silicates in chesterite from metamorphosed ultramafic rocks from Chester, VT, allowed confirmation of these building principles (Veblen and Burnham 1978a, b).

Early studies of silicates using high-resolution transmission electron microscopy (HR TEM) (Buseck and Iijima 1974) have shown the feasibility of the method to underpin chain-width

disorder, intergrowths, microstructures, and reaction mechanisms between pyriboles and sheet silicates (Veblen and Buseck 1979, 1980, 1981). These studies provided a systemized approach to pyriboles that defines 'zippers' (slabs of a different chain-width to a host pyribole) and their terminations considered to obey two theoretical rules: "*Rule l: the terminating zipper must have the same number of sub-chains as the material it replaces. Rule 2: the numbers of silicate chains in the zipper and in the material it replaces must both be even, or they must both be odd"* (Veblen and Buseck 1980).

Inspired by the idea that biopyriboles play a key role in understanding petrogenetic processes spanning igneous and metamorphic environments and across a broad range of geological settings and epochs, HR TEM studies of natural and synthetic materials have addressed pyriboles and NCPs polysomatic intergrowths and their formation (e.g., Cressey et al. 1982; Akai et al. 1982, 1997; Yau et al. 1986; Schumacher and Czank 1987; Droop 1994; Grobéty 1996, 1997; Najorka and Gottschalk 2003; Ams et al. 2009; Konishi et al. 2008, 2010; Ferrari and Viti 2010). An overview of experimental synthesis and compositional limits of monoclinic triple chain silicates was provided by Jenkins et al. (2012).

Ciobanu et al. (2022) used high angle annular dark field (HAADF) scanning TEM (STEM) instead of conventional bright field (BF) TEM imaging technique to show an unusual assemblage of NCPs (triple-chain silicate as zippers within ferro-tschermakite) occurring as nanoinclusions hosted by magnetite from Wirrda Well (South Australia). This study provided a basis for interpreting NCP structures that allowed enhanced similitude to crystal structure models than the BF TEM imaging technique.

Magnetite is an early mineral in iron oxide copper gold (IOCG) deposits and is preserved as the dominant Fe-oxide if the system does not evolve to hydrolytic-hematite alteration. Magnetite is

representative of main ore stages in deposits from some of the world's largest IOCG terranes, such as the Neoarchean Carajás Mineral Province, Brazil (e.g., Monteiro et al. 2008; Schutesky and de Oliveira 2020; Veloso et al. 2020; Campo-Rodriguez et al. 2022). In the giant Mesoproterozoic Olympic Cu-Au Province of South Australia, however, magnetite is restricted to deeper and outer margin of orebodies (Ciobanu et al. 2019, 2022; Verdugo-Ihl et al. 2020, 2021). Nanoscale studies of hydrothermal magnetite have shown this mineral can contain abundant inclusions of various types, including spinels, calc-silicates, etc., and that these inclusions represent valuable evidence that can help validate genetic models (Ciobanu et al. 2019, 2022; Verdugo-Ihl et al. 2021).

Magnetite from the Carajás province has also been shown to host nanoscale inclusions (Huang and Beaudoin 2021; Huang et al. 2022). In this study we employ HAADF STEM to characterise silicate inclusions in magnetite from the Jatobá Cu-Ni deposit in the Carajás province. Jatobá is one of many IOCG deposits in the Carajás Province hosted along a major shear zone within mafic-ultramafic sequences (Veloso et al. 2020). Considering that a majority of reported occurrences of NCPs derive from altered mafic/ultramafic complexes (Veblen and Burnham 1978a, b; Cressey et al. 1982; Schumacher and Czank 1987; Droop 1994; Grobéty 1996, 1997; Akai et al. 1997; Konishi et al. 2008, 2010; Ferrari and Viti 2010), we aim to find whether NCP are present in Jatobá magnetite. In addition, we raise the question whether magnetite preserves silicate inclusions typical of IOCG alteration like those described by Ciobanu et al. (2019, 2022). Systematic investigation of magnetite from ore deposits opens a compelling path to better understand NCPs, their polysomatic sequences, and inherent chain-width disorder beyond the classical occurrences known from amphiboles in country rocks.

ANALYTICAL METHODS

Two thin polished sections of magnetite-bearing samples were studied at the nanoscale: (i) chalcopyrite-rich ore sample (Jt7); and (ii) altered mafic/ultramafic rock (Jt10). The two samples are from the same drillhole (DH0032), 60 meters apart. Sample characterization comprised reflected light optical and scanning electron microscopy (SEM) using a FEI Quanta 450 instrument operated in back-scattered electron (BSE) mode to assess magnetite grains and select areas for nanoscale investigation. Three S/TEM (<100 nm) foils were prepared from the sections using a FEI-Helios nanoLab Dual Focused Ion Beam and SEM (FIB-SEM) as outlined by Ciobanu et al. (2011). Each foil was analyzed employing HAADF STEM imaging and energy-dispersive X-ray spectrometry (EDS)-STEM mapping using an ultra-high resolution, probe-corrected, FEI Titan Themis S/TEM operated at 200 kV. This instrument is equipped with a X-FEG Schottky source and Super-X EDS geometry. The Super-X EDS detector provides geometrically symmetric EDS detection with an effective solid angle of 0.8 sr. Probe correction delivered sub-Ångstrom spatial resolution and an inner collection angle greater than 50 mrad was used for HAADF imaging with a Fischione detector. Velox software was used for image acquisition, including drift-corrected frame integration package (DCFI), and EDS data acquisition and processing. Various filters were used to eliminate noise. Quantification of the collected EDS spectra was performed using Thermo-Scientific Velox software (v3.10) which utilizes standard Cliff-Lorimer quantification and included absorption correction optimized for both the Super-X detector geometry and also the effect of sample holder shadowing for the double-tilt Super-X holder used. Quantification was performed using the Brown-Powell empirical ionization cross-section model and uncertainty values reported incorporate an estimated 20% error in the k-factors. Calculation of mineral formulae was performed using a spreadsheet adapted from Ridolfi et al. (2018). Indexing of diffraction patterns was conducted with WinWulff© (JCrystalSoft) and publicly available data

from the American Mineralogist Crystal Structure Database (http://rruff.geo.arizona.edu/AMS/amcsd.php). Crystal structure models were generated in CrystalMaker® and image simulations using STEM for xHREM™ software. Empirical models were derived by using 'slicing and merging' modules of known structures using CrystalMaker software. All instruments are housed at Adelaide Microscopy, The University of Adelaide.

RESULTS

Nanoscale inclusions in magnetite

In both samples, magnetite is manly associated with sulfides (chalcopyrite and pyrite), biotite, chlorite, and quartz; apatite is an abundant component (Fig. 1a, b). Magnetite is a relatively minor component of the ore sample where it displays a banded texture with respect to sulfides and gangue minerals. In contrast, magnetite is a major component (>75%) of the altered lithology, where it forms massive lenses. The magnetite has a subhedral morphology (Fig. 1c, d), albeit slightly deformed and more marginally corroded by gangue and sulfides than in the ore sample. Magnetite is characterized by abundant inclusions (e.g., silicates, sulfides, and ilmenite), is partially fractured, and displays irregular domains of enhanced porosity.

The distribution of silicate inclusions varies from scarce in the ore sample to abundant in the altered mafic/ultramafic rock (Fig. 1e, f). In the ore sample, silicates form acicular <111> networks in magnetite and these are crosscut by ~10-20 μm-wide bands with mottled, finer inclusions (Fig. 1e). Densely mottled cores are found in the magnetite from the mafic/ultramafic sample (Fig. 1f). In detail, a concentric pattern of inclusions is observed around relatively coarser (20-30 μm-sized) grains of ilmenite. Towards the edges, the mottled area displays irregular domains with coarsening of the silicate inclusions (Fig. 1f). The three S/TEM foils for nanoscale study were prepared from

slices cut by FIB placed across areas with densest inclusions (Fig. 1e, f). One slice was cut across the boundary between magnetite and ilmenite to establish whether this is accompanied by ulvöspinel and/or other spinel phases.

The foils (Online Materials Fig. A1) show that the distribution of inclusions at depth is comparable with that observed on the magnetite surface, i.e., scarce, and densely mottled, respectively, for grains from the two samples. The inclusions are silicates, without any spinels present, although an inclusion-free area is observed adjacent to the ilmenite boundary. The silicate assemblage is dominated by amphiboles, with minor biotite, talc and chlorite, and trace titanite and allanite. In addition, Si-rich blebs or square-shaped inclusions are present, some of which also contain Mg and are amorphous. The foil from sample Jt7 shows amphiboles as two long (μm-sized), acicular grains parallel with one another and an isolated, stubby aggregate of different orientation. In contrast, foils from sample Jt10 feature clustered nm-scale amphibole inclusions of comparable orientation interspersed with larger clots of amphibole, each several hundreds of nm in length. In the foil obtained across the ilmenite/magnetite boundary, a longer, micron-sized, inclusion of mica/chlorite (?) crosscuts the amphiboles but this was plucked out during FIB milling.

A selection of aggregates and amphibole grains are shown in Figure 2. The aggregates, up to 1 μm in length, show rectangular and elongate shapes attributable to different orientations relative to the plane of view (Fig. 2a). Some are associated with an amorphous Si-(Mg)-rich phase or are partially mantled by diverse talc+chlorite+biotite assemblages (TCB) and minor titanite. Sub-rounded grains are interspersed among the dominant population of thin, prismatic amphiboles (Fig. 2b, c).

This is the peer-reviewed, final accepted version for American Mineralogist, published by the Mineralogical Society of America.
The published version is subject to change. Cite as Authors (Year) Title. American Mineralogist, in press.
DOI: https://doi.org/10.2138/am-2023-9188. http://www.minsocam.org/

Common to all inclusions are lamellar intergrowths readily seen as irregular rhythms of bright and dark bands on HAADF STEM images. Such intergrowths always contain slabs displaying the crystal structure of amphibole (see below), which correspond to the brighter bands. The darker bands are composed of irregular sequences of other chain silicates, spanning a wide range of I_{beams}, from conventional pyriboles (pyroxene and amphibole) to NCPs such as clinojimthompsonite and (clino)chesterite. Intergrowths patterns vary widely from one case to another and are more pronounced in the subhedral grains (Fig. 2b) whereas the thin amphiboles display only a few such bands (Fig. 2c). Parts or grains forming the aggregates can also lack such banding. A second peculiarity is the rhythmic zoning across the grain elongation observed as bright or dark strips on the HAADF STEM images. Some grains combine domains with and without lamellar intergrowths (see below).

Compositions obtained from STEM mapping of inclusions of all types are given in Online Materials Tables 1 and 2 and plotted on Figure 2d. The data was obtained from integrated spectra over areas without (or with only negligible) intergrowths, but over the entire grains whenever they are banded. The overall composition of grains with lamellar intergrowths are also given relative to amphibole-only areas selected from the same grains. There are two main categories: calcic (actinolite, magnesio-hornblende and (ferro)tschermakite); and Mg-(Fe)-amphiboles (cummingtonite) (Fig. 2d). We note the ratio of cations (Me) in B and C sites $^{B}Me/^{C}Me$ is close to ideal 2/5=0.4 for all except one calcic amphibole (0.33 for analysis #10-bottom in Table 1 Online Materials). The upper, Mg-(Fe) amphibole of the same inclusion also has lower $^{B}Me/^{C}Me$ ratio (0.31 for analysis #10-top in Table 2 Online Materials). Lower $^{B}Me/^{C}Me$ ratios are also obtained for Mg-(Fe)-amphiboles with the densest NCP intergrowths from the four aggregates (mean=0.34;

Online Materials Table 2). However, the mean ratio becomes 0.38 when obtaining compositions from selected areas/bands without intergrowths from the same aggregates.

(Ferro)tschermakite containing up to 14.9 wt.% Al_2O_3, is identified from the largest, acicular inclusions in the ore sample. (Ferro)tschermakite displays the highest A site occupancy, with the average composition: $^{A}(Ca_{0.43}Na_{0.27}K_{0.13}v_{0.17})_1{}^{B}(Mg_{0.44}Ca_{1.56})_2{}^{C}(Fe^{2+}{}_{1.94}Mg_{1.45}Al_{0.9}Fe^{3+}{}_{0.7}Ti_{0.02})_5{}^{T}(Si_{6.37}Al_{1.64})_8\,O_{22}(OH)_2$.

Most of the amphiboles in the aggregates that lack lamellar intergrowths correspond to actinolite, except for magnesio-hornblende in aggregate 1 from the ore sample.

Intriguingly, a single grain (Fig. 2c, d) imaged throughout as dominantly amphibole (see below) and plotting in the field of magnesio-hornblende, contains 6.7 wt.% Ce_2O_3. The calculated empirical formula for this Ce-bearing amphibole is: $^{B}(Ca_{1.66}v_{0.34})_2{}^{C}(Mg_{2.37}Fe^{2+}{}_{1.11}Al_{0.64}Fe^{3+}{}_{0.53}Ce_{0.36})_5{}^{T}(Si_{7.16}Al_{0.84})_8O_{22}(OH)_2$.

The effect introduced by the presence of chain width disorder on measured compositions in the two analysis #10 were assessed using the method of Bozhilov et al. (2007). Calculated $^{B}Me/^{C}Me$ ratios are 0.37 and 0.289 for #10 top and -bottom, respectively (Fig. A2 Online Materials). These values show 0.06 and 0.04 difference to the measured ratios implying the EDS STEM data is reliable.

For the sake of comparison, compositions obtained from the entire grains with lamellar intergrowths in the four aggregates were also plotted assuming an overall amphibole crystal chemistry (Fig. 2d). These show an increase in Mg content relative to the non-banded parts, except for one case (Aggregate 2) in which Fe-enrichment is observed. The part of the Ce-bearing amphibole featuring dense intergrowths also plots in the cummingtonite field, like the aggregates.

The same grain also shows an association between a calcic (Ce-bearing) and Mg-(Fe) amphibole, like the paired composition of amphiboles in the aggregates.

The lamellar intergrowths within single grains or amphibole aggregates are shown in closer detail in Figure 3. Such intergrowths can be continuous along the length of the grain, irrespective of whether the inclusions are rounded or subhedral (Fig. 3a, b). A relative increase in Mg within grains from aggregates correlates with NCPs as darker bands in the lamellar intergrowths (Fig. 3c-g). Some aggregates also show changes in composition, from Ca-to Fe-rich zones across lamellae of variable rhythms (Fig. 3c). Calcium-rich strips across the intergrowths are observed in other cases (Fig. 3d). Direct contacts between actinolite and cummingtonite (and associated Mg-richer intergrowths) are depicted in aggregates 2 and 4 (Fig. 3e, f). Highlighting the complexity between the textures and chemical changes in the inclusions are Fe-rich strips that crosscut actinolite (Fig. 3f) and the observed changes in Ca/Fe ratio along the same bands within a lamellar intergrowth (Fig. 3g).

EDS STEM maps were generated to further constrain compositional variation, intergrowths, and zonation patterns among amphiboles (Figs. 4, 5; extended maps in Online Materials Figs. A3-A4). Maps of larger areas with densely mottled inclusions show the two distinct populations of amphiboles (Ca- and Mg-rich: Fig. 4a). Tiny Ce-bearing inclusions are present, close to, or attached to amphibole grains (inset in Fig. 4a). An association between calcic (actinolite) and Mg-(Fe)-amphibole (cummingtonite), typical of the aggregates (Fig. 4b, c) is partially replaced by TCB along straight or scalloped boundaries. The rhythms of bright bands (amphibole) in an intergrowth are mimicked by the variation in Fe concentration (Fig. 4c).

EDS STEM mapping of the binary inclusion comprising cummingtonite and Ce-bearing magnesio-hornblende (bottom) shows a rhythmic zonation with respect to Ca and Fe across the

banding in the cummingtonite (top of Fig. 5a) whereas Ce and Al are evenly distributed only throughout the Ce-bearing magnesio-hornblende (bottom of Fig. 5a). Calcium and Mg are present across both grains, whereas Fe is enriched in cummingtonite. EDS STEM element maps of (ferro)-tschermakite and associated biotite show the amphibole is not zoned with respect to Ca, Al or Mg, and contains measurable Na (Fig. 5b). Notably, Ti is enriched in the mica and to a lesser degree in the enclosing magnetite relative to the amphibole (Online Materials Fig. A4).

NANOSCALE CHARACTERIZATION

Crystal structures of chain silicates

Interpretation of high-resolution HAADF STEM images is dependent upon fitting crystal models with simulations onto projections that are relevant for identification of specific motifs and how those motifs adapt to structural modularity. The atoms on such images are observed as dots of variable size and intensity (I), in turn controlled by atomic number of each element ($I \sim Z^2$), site occupancy, and their density along the atomic columns perpendicular to the view plane.

In a simplified sense, all chain silicate structures display a central ribbon of atoms representing the *C* cations (octahedral coordination), bordered by two *B* cations (dodecahedral) at the ribbon edges (Fig. 6). Pairs of Si-tetrahedra (*T*) flank the ribbon on both sides and their number is considered for the I_{beam} notation of each species: 2 for amphibole; 3 for clinojimthompsonite; and 2 combined with 3 for chesterite (Veblen and Burnham 1978b). The *A* cations are located at the edges of the central ribbon and between each pair of T cations.

Whereas the number of *B* cations remains unchanged, the increase in the number of *C* and *A* cations from amphibole to n chain silicates (nI_{beam}) can be expressed by the formula:

$$(1)\ nI_{beam} = T(2+n) = C(5+3n) = A(1+n), \text{ where n is an integer.}$$

The increase in the number of C and T cations controls expansion of the *b* unit cell parameter (by ~9 Å per additional I_{beam}). The *a* and *c* parameters remain relatively constant.

The same formula is valid for polysomes of chain silicates combining two or more I_{beams}, in which the structure results from addition of elements within the component units. For example, chesterite (2- and 3-I_{beams}), the only polysome for which the crystal structure has been determined (Veblen and Burnham 1978b), is orthorhombic (space group $A2_1ma$), and thus distinct from the monoclinic space groups ($C2/m$ and $C2/c$) of the other chain silicates discussed here. The modular structures of chain silicates can be compared when projected on [001] zone axis. For consistency, polysomatic sequences of NCP and amphibole were also imaged on three additional zone axes: $[10\bar{2}]$; $[10\bar{1}]$; and [101] (Figs. A6-7 Online Materials) by tilting along the *b* axis. Imaging of Ca-Al-amphibole (Fts) on [010] zone axis shows no disorder (Fig. A8 Online Materials).

The above description of crystal modularity is shown using actinolite (Evans and Yang 1998), clinojimthompsonite and chesterite (Veblen and Burnham 1978b) as illustrative structures of 2-, 3- and (23) chain silicates, respectively (Fig. 6). STEM simulations for these structures show a good match with the atom fill models, whereby the *B* and *C* cations are recognized as bright dots of variable intensity and flanked by the *T* cations. In the cases selected here, the *B* cations are brighter than the *C* cations due to their relative atomic mass, e.g., Ca (Z=20) compared to Mg (Z=12) in actinolite. The *A* sites, which host Na and/or K cations, but with very low occupancy in actinolite (K+Na=0.037) and missing altogether in clinojimthompsonite and chesterite, are depicted as black, diamond-shaped motifs. Beneath the models and simulations, we show a selection of HAADF STEM images [on different zone axes] illustrating the same structures (Fig. 6) and their excellent fit with the models.

This is the peer-reviewed, final accepted version for American Mineralogist, published by the Mineralogical Society of America.
The published version is subject to change. Cite as Authors (Year) Title. American Mineralogist, in press.
DOI: https://doi.org/10.2138/am-2023-9188. http://www.minsocam.org/

Using equation (1) above and existing structures for actinolite and clinojimthompsonite, we have generated 4- and 5-I_{beam} models to illustrate how the appearance of the structures change systematically on HAADF STEM images as cell size increases (Fig. 6). We note that the monoclinic I_{beam} structures with even and uneven number are likely to correspond to *C*2/*m* and *C*2/*c* space group types, respectively, or a corresponding subgroup. The STEM simulations for each structure clearly show the number of atoms along the ribbon, the *T* pairs, and the diamond-shaped black motifs.

Pyroxene, the simplest I_{beam} structure (1) is also observed but only as single slabs, or zippers, that occur within sequences of other chain silicates, mostly 2- and 3-I_{beams} (Fig. 7a, b). Pyroxene has 4 cations along the central ribbon (with two *C* cations and two *B* cations at the ribbon edges) flanked by a single pair of Si-tetrahedra (*T*). There are no *A* sites (Fig. 7c). Such structure can be joined along $(010)_{planes}$ with other chain silicates by *a*/2 offset of the pyroxene central ribbon relative to that in the host silicate (Fig. 7c, d). The structures and I_{beam} schematics illustrate the resulting zipper sequences displaying two types of alternating $(010)_{planes}$ with *a*/2 periodicity along *b*: (i) (212) and (213) and (ii) (2gap2) and (2gap3). The gap links adjacent *B* cations in the host structures and stands for a narrower interval than their *A* site(s) (Fig. 7c, d).

A sequence with abundant pyroxene zippers within amphibole (Fig. 7e) illustrates the additional in such intergrowths. Notable in this example is the presence of 5-I_{beam} zippers forming polysomatic intergrowths with 1-, 2- and 3-I_{beam} slabs.

Sequences of polysomatic intergrowths

This is the peer-reviewed, final accepted version for American Mineralogist, published by the Mineralogical Society of America.
The published version is subject to change. Cite as Authors (Year) Title. American Mineralogist, in press.
DOI: https://doi.org/10.2138/am-2023-9188. http://www.minsocam.org/

Assessment of polysomatic intergrowths over longer length intervals, from 60 to ~250 nm from three aggregates in Figures 2, 3, 8, and Online Materials Figure A5 shows these have I_{beam} averages ($\bar{I}_{beam}$) around 2.5-2.6. These were calculated using the formula:

$$(2)\quad \bar{I}_{beam}=\Sigma n I_{beam}(i)/N I_{beam},$$

where n=number of each I_{beam} of index (i), and N=total number of I_{beams} in the sequence. This implies that the composition of such grains lies between that of Mg-Fe amphiboles and clinojimthompsonite, as confirmed by their locations on Figure 2d. Most of these sequences show polysomes with combinations between 3-I_{beam} and other NCPs (4- to 6-I_{beams}) within host amphibole.

The longest sequence, 247 nm (Online Materials Fig. A5) is from aggregate 1 and shows rhythms between amphibole and polysomes dominated by the 3-I_{beam}. Shorter sequences from the same aggregate show I_{beams} that average to comparable dimensions as in the longer profile (Fig. 8a, b). There are, however, differences between parts of the grain that are Ca- or Mg-rich ($\bar{I}_{beam}$ size 2.22 and 2.63, respectively; Fig. 8a). The Fe-rich profile shows a greater number of higher order NCPs (Fig. 8b), concordant with the increased in $\bar{I}_{beam}$ size. The polysomes are always highly irregular and can change sequence across the Ca-rich/Fe-rich boundary where zipper terminations within the polysomes are common (Fig. 8a, c). Comparable features are illustrated in Fig. 8c, d from ~100 nm-long profiles obtained from two other aggregates that also display compositional boundaries. In the Fe-rich part of aggregate 2, one side is dominated by a greater abundance of 3-I_{beam} structures, whereas the other shows NCP zippers terminated either below or at the boundary to the Ca-rich part (Fig. 8c). In contrast, the 3-I_{beams} traverse the composition boundary.

Profile 4 from aggregate 3 displays simpler polysomes with sequence changes and defects rather than terminations across the Ca-rich/Fe-rich boundary (Fig. 8d). A range of such sequence changes and zipper terminations are shown in Figure 8e, f.

The most abundant population of inclusions is represented by amphibole with zippers comprising various pyriboles or NCPs (Fig. 9). Such zippers mostly extend along the entire length of the grain but can also display terminations and defects related to Fe-rich compositional bands (Fig. 9a). Otherwise, thin rhythms of Fe banding (<5 nm-wide) are observed within regular amphibole sequences (Fig. 9b, c). The Fe-banding can cross over triple-chain or pyroxene zippers in amphibole (Fig. 9c, d). We note the presence of (1233) polysome as one of the more complex zippers within amphibole (Fig. 9d). Epitaxial relationships between $[11\bar{2}]_{magnetite}$ and $[001]_{amphibole}$ are shown in Figure 9e.

The Ce-bearing amphibole (Fig. 9f) shows a highly ordered 2-I_{beam} sequence with some disorder towards the margins represented by intergrowth of single pyroxene or triple 3-I_{beam} structures (Fig. 9g). Fast Fourier transform (FFT) patterns (insets in Fig. 9c, f) indicate these amphiboles have monoclinic symmetry. The other part of the Ce-bearing amphibole shows more complex polysomes that include 4- and 5-I_{beam} NCPs (Fig. 10h).

Several polysomatic sequences display wider, rhythmic intergrowths between amphibole and the triple chain silicate (Fig. 10a, b). Blocks of 10 or 11 rows of 2-I_{beam} are interspersed with blocks of up to 8 rows of 3-I_{beam} in sequences dominated by amphibole, which nonetheless show domains of chain disorder (Fig. 10a). A switch to sequences dominated by triple chains is noted in the grain from Figure 3a, in which a block of 19 rows of 3-I_{beam} structure is flanked by finer rhythms of both 2- and 3-I_{beam} intergrowths (Fig. 10b). This block becomes wider (up to 23 rows of 3-I_{beam}) and shows NCP zippers as single rows of 5-I_{beam} structures (Fig. 10c). The FFT pattern indicate a

This is the peer-reviewed, final accepted version for American Mineralogist, published by the Mineralogical Society of America.
The published version is subject to change. Cite as Authors (Year) Title. American Mineralogist, in press.
DOI: https://doi.org/10.2138/am-2023-9188. http://www.minsocam.org/

monoclinic structure corresponding to clinojimthompsonite. There is also a very good match between the HAADF STEM image and the clinojimthompsonite simulation (Fig. 10d). In detail, combinations of (523) or (235) mark the end of the wider block in the center of this clinojimthompsonite grain (Fig. 10e, f).

NCP-bearing polysomes (e.g., aggregate 4 shown in Figure 3e) are highly disordered and display I_{beams} in the range of 4 to 7 within hosts of triple and double-I_{beam} structures (Fig. 11a). We note however the presence of repeats such as (737) or (5656), the latter being terminated on one side by a (354) I_{beam} sequence. Higher I_{beam} structures, 11 and 12, form single zippers with changes in size along $(010)_{planes}$ (Fig. 11b, c). For example, the 11-I_{beam} becomes a (335) sequence, and the 12-I_{beam} becomes a (93) sequence. In addition, we note the presence of 5- and 6-I_{beams} zippers associated with rows of 3-I_{beams} in the same locations as such wide NCPs. None of these NCP-bearing polysomes form regular repeats. Details of the NCPs identified are shown in Figure 11d spanning the entire range from 4- to 7-, and 9-, 11-, 12-I_{beam} structures. 8- and 10-I_{beam} structures are not observed within the longer polysomes.

Defects

A wide range of defects are present throughout the studied chain silicates (Figs. 12, 13). Larger fields of amphibole with more regular zipper sequences comprising double or triple rows of 3-I_{beam} structures display chain derailment, sequence changes, or loops with simple or hairpin geometry and terminations (Fig. 12a). A glossary of defect structures is provided in the online materials. These chain modifications are abundant in areas where single NCPs are included within 3-I_{beam} zipper sequences. Planar defects are represented by sets of normal and inverse faults that can run over tens of nm and which link different zipper sequences (Fig. 12a, b). Simple derailments are relatively rare, more commonly they are associated with “jogs”, shorter defects assisting chain

dislocation and in some cases sequence inversion (Fig. 12c). Short displacements are produced by conjugate, oblique sets of defects, crossing over up to as many as ten to twelve chains (Fig. 12d). In detail, these are low-angle defects with step-displacements along their trajectories.

Formation of 8- and 10-I_{beam} structures is observed in sequences involving NCP zippers with chain defects (Fig. 12e, f). Three ribbons of 8-I_{beam} silicate occur along the derailment of a quadruple zipper (Fig. 12e). A 10-I_{beam} structure (Fig. 12f) is observed along an unusually wide NCP zipper with multiple width changes, from 15-I_{beam} structure to evolving polysome sequences: (627) → (62.11) → (62.10) (Fig. 12d). Schematics in Figure 12g and h show details of the 8- and 10-I_{beam} structures.

En-echelon defects are also noted across some NCP zipper sequences (Fig. 13a). An unusual coherent zipper change is the sequence switch from (226) to (523) polysomes taking place along the *b* axis without any displacement. On the other side of the zipper sequence displaying the *en-echelon* defects, we note that a change from (326) to (22223) polysomes is assisted by an asymmetric "bow" defect.

Other, less common defects are those linking multiple NCP zippers (Fig. 13b). Such defects assist local changes in sequence and/or terminations. Details of the oblique defects and jogs are shown in Fig. 13c, d). The jogs show *b*/2 displacements of the chain silicate, e.g., the switch between 4- and 3-I_{beam} chains shown in Figure 13d. We note changes in the HAADF signal intensity along the ribbon accompanying such jogs.

A further type of defect which is associated with distortion in the host silicate involves 'swells' between adjacent NCPs and/or pyriboles (Fig. 13e, f). Such swells result in *a*/2 disruption of the chains across the defects. The swell can be either single or double step, e.g., across sequences with

This is the peer-reviewed, final accepted version for American Mineralogist, published by the Mineralogical Society of America.
The published version is subject to change. Cite as Authors (Year) Title. American Mineralogist, in press.
DOI: https://doi.org/10.2138/am-2023-9188. http://www.minsocam.org/

changes from 12- to (93)-I_{beam} or from (532) to (46)-I_{beam}. The two types of swells are shown schematically in Figure 13h, g.

Both coherent and incoherent terminations are observed for short NCP zippers (Fig. 13i, j). Coherent, arcuate terminations of multiple zippers are also noted, such as the (32423) sequence shown in Figure 13k. The I_{beam} schematic of the switch between I_{beam} zippers is shown in Figure 13l.

Sheet silicates

High-resolution imaging of the aggregates displaying marginal replacement such as those shown in Figure 4b, c, confirms the presence of sheet silicates represented by talc, biotite, and chlorite in direct contact with chain silicates (Fig. 14). Integrated EDS spectra for the three species are shown in Online Materials Fig. A9. The replacement boundary can display a ragged outline with $talc_{[100]}$ (also identified from the FFT pattern in the figure inset) forming inliers along the *a* axis of the $amphibole_{[001]}$ (Fig. 14a). The direct contact is marked by voids (?) occurring as black motifs along common <010> directions. Displacement of 7-I_{beam} zippers within the amphibole are noted along jog-type defects. Straight contacts along <010> directions are also common between sheet and chain silicates (Fig. 14b). Changes from talc to mica sequences are observed on one of the stepwise <110> margins exposing coherence between cation ribbons in the two types of silicates along <010> directions. The FFT pattern obtained from the area confirms the crystallographic alignment between them (inset in Fig. 14b).

NCP polysomes evolving from (253322623) to (15.13) sequences show a transition to the talc structure marked by slight corrugation of the sheet silicate (Fig. 14c). Swell-type defects are present in the talc. Replacement of amphibole by talc along two directions, <100> and <010>, also

This is the peer-reviewed, final accepted version for American Mineralogist, published by the Mineralogical Society of America.
The published version is subject to change. Cite as Authors (Year) Title. American Mineralogist, in press.
DOI: https://doi.org/10.2138/am-2023-9188. http://www.minsocam.org/

shows a straight outline, albeit with stepwise geometry on one side (Fig. 14d). Defects in the talc sequence are marked by a patch of chlorite. Straight contacts along <010> directions between mica (biotite) and amphibole (actinolite) are also coherent (Fig. 14e).

Sequences of talc and chlorite are also observed (Fig. 14f). The FFT pattern of chlorite is distinct from both talc and mica on the [100] zone axis (Fig. 14f inset). Swelling defects and transition between talc and other sheet silicates is very common (Fig. 14g).

The changes in the HAADF STEM images between the three sheet silicates are highlighted by atom-fill models (Fig. 14h-j). Although the FFT patterns for talc and mica are undistinguishable on [100] zone axes (Fig. 14a, e), the HAADF STEM image shows a 'dot' between the T sites (Fig. 14e), representing the K atoms in the mica structure (Fig. 14h). On the other hand, the sandwich type structure of chlorite$_{[100]}$ displaying cation ribbons flanked by alternating T and OH modules (Fig. 14i) is also visible on the HAADF STEM images (Fig. 14d, f). Talc has the simplest structure (Fig. 14j). This is reproduced by STEM simulations (overlay in Fig. 14f) with relatively good fit to the images.

DISCUSSION

Polysomatic and chain-width disorder: primary versus replacement reactions

We attribute the observed features to co-crystallization of double- and triple-chain silicate structures since the majority of the polysomatic sequences we observe are constrained within comparable $\bar{I}_{beam}$ ranges between 2 and 3-I$_{beams}$, despite their wide variation across or along a single grain (Figs. 3a, b, 8). Although some grains record wider intergrowths of 2- and 3-I$_{beam}$ structures, neither the larger blocks nor the finer scale intergrowths form regular repeats (Fig. 10). Therefore, polysomatic disorder is the main feature of the chain silicate packages described here.

Nonetheless, the presence of rhythmic intergrowths, either as blocks (Fig. 10a, b), or short 3-I_{beam} sequences within amphibole (Fig. 9f), indicates that the crystallization process is self-organized at a scale of hundreds-of-nm intervals rather than randomly.

Primary co-crystallization is also inferred from the fact that the NCPs, either as single or more complex zippers, form along the entire length of the crystal. However, changes in the sequences along the crystal, and in particular, terminations of wider zippers, are indicative of polysomatic reactions between different I_{beam} sequences (Figs. 3g, 8, 9f). This is especially true in the aggregates enveloped by sheet silicates in which the widest NCP sequences are recorded (Figs. 2a, 11, 14).

Additionally, disorder is defined by the fact that polysome ranges across any given profile are always combinations of wider (up to 13- discrete I_{beam} structures) with shorter (down to single I_{beam} structures) sequences (Fig. 8). Although all the polysome sequences do not show repeats of sufficiently long range to enable definition of specific species, we note the presence of the 5-I_{beam} as a polytype of the (23)-I_{beam}, albeit as single zippers or as a component of multiple zippers (Fig. 10e, f).

The presence of wider chain silicates as metastable phases during the replacement of amphibole by talc (Veblen and Buseck 1980) is a viable interpretation for the widest NCP polysomes reported here as ‘fronts’ protruding from the sheet silicates (Fig. 14a, c). However, the observed formation of isolated NCPs across longer sequences of double and/or triple chain silicates are attributable to kinetic instabilities developed during primary growth that result in coherent zipper terminations within host structure (Figs. 8, 10). Some of the widest chain sequences documented by us (Fig. 11) can be linked to kinetic models involving increasing and decreasing chain-width during primary formation of the triple-chain silicate (Grobéty 1997). Such schemes invoke ‘species’ mobility by

side-stepping glide mechanisms along the *b* direction (e.g., triple chain zipper displaying a 4-step derailment in amphibole; Fig. 8f).

Chain-width disorder is also widely represented in the studied material and can be discussed in terms of the two rules of coherent zipper termination (Veblen and Buseck 1980). Although the polysome sequences obey these rules (Fig. 8e), breaches are common, particularly in areas with defects associated with wider I_{beam} structures.

Violation of rule 1 (sub chain number N_i) is found when displacive planar faults or short jogs transform sequences with non-matching N number on the two sides of the defects, e.g., N_1=11(2333) → N_2=12(3333) (Fig. 13c), or N_1=10(424) → N_2=9(333) (Fig. 13d). Moreover, violation of rule 1 is also encountered along zippers that change in width without planar defects as we show in Figure 12e-h for the occurrence of 8- and 10-I_{beams}. For example, the 8-I_{beam} is placed both between sequences with N_1=8(422) and N_2=6(222), or with N_2=10(2224), depending on how the length of the sequence is selected (Fig. 12g). Terminations of a single 6-I_{beam} zipper leads to sequences such as N_1=6(222) and N_2=7(232) (Fig. 13j), also infringing on rule 1.

Examples of single zippers doubling (12-I_{beam} → (93), or double zippers changing into triple zippers (46) → (532) (Fig. 13e, f) break rule 2, since the zipper numbers are not both either even or uneven. Notably, these changes are not associated with zipper terminations or planar defects.

Even more common are examples in which both rules are violated. For example, the *en-echelon* zippers shown in Figure 13a feature a 6-I_{beam} on one side changing into a (32) sequence, and a 5-I_{beam} becoming a (22) sequence, both with non-conserved N (Fig. 13l). In contrast, the other side of the same *en-echelon* structure displays conservative changes from N_1=11(32222) to N_2=11(326). A further example that breaks both rules occurs along the inverse fault illustrated in Figure 12b. This shows a single 5-I_{beam} changing to a double (22) zipper and a quadruple zipper of

This is the peer-reviewed, final accepted version for American Mineralogist, published by the Mineralogical Society of America.
The published version is subject to change. Cite as Authors (Year) Title. American Mineralogist, in press.
DOI: https://doi.org/10.2138/am-2023-9188. http://www.minsocam.org/

N_1=11(3233) changing to a quintuple zipper of N_2=10 (22222). We note that the terminations of the 5-I_{beam} zippers are those which most commonly break the conservation rules (Figs. 8f and 11b, e).

The occurrence of planar faults and other defects during replacement reactions among pyriboles is concentrated in regions of chain-width disorder with violation of the two termination rules (Veblen and Buseck 1980). However, primary growth was also invoked either for the formation of isolated wider chains in amphibole (Cressey et al. 1982), or for the simultaneous growth of NCPs with rule violation (Konishi et al. 2010). The NCPs discussed here are outstanding examples of chain-width disorder with defects disobeying the terminations rules. Among these defects, jogs, swells, oblique/low-angle and *en-echelon* faults are indicative of strain-induced deformation during growth. Violation of the two rules and, especially, the lack of planar displacive faults accompanying chain-width disorder in pyriboles intergrown with anthophyllite was interpreted as associated with metamorphic deformation of host lithologies by Konishi et al. (2010) in their study of Archean ultramafic rocks from Greenland.

The relationships between chain and sheet silicates indicate coherent grain replacement (Fig. 14) as discussed by Veblen and Buseck (1980). This is represented by grain boundaries in which transition from (010) to (100) takes place via (210) interfaces (Fig. 14b, d). Nevertheless, the (210) interface also shows stepwise displacement where the sheet silicate changes from one species to another (talc to mica or chlorite). We also note the presence of either single or double ledges between amphibole and talc along the (100) interface (Fig. 14a, g). Features along this interface, which we interpret as channels, are clearly visible on HAADF STEM images (Fig. 14a, b, e).

Chemical patterning and fluid evolution recorded by chain silicates in magnetite

The two groups, calcic and Mg-(Fe) amphiboles (Fig. 2d), indicate distinct generations of inclusion growth in magnetite. Among these, the presence of Al-rich and Ce-bearing calcic amphibole is indicative of variable physical-chemical conditions (high pressure for ferrotschermakite) or REE-enriched fluid sources. Moreover, the concentration of NCPs in Mg-Fe- rather than calcic amphiboles in the altered mafic/ultramafic rock hints at the better preservation of a geochemical signature inherited from the host lithology in the former. This correlates with the preferred affiliation of NCPs with altered and/or metamorphosed mafic-ultramafic complexes noted in the literature (e.g., Veblen and Burnham 1978a, b; Cressey et al. 1982; Schumacher and Czank 1987; Droop 1994; Grobéty 1996, 1997; Akai et al. 1997; Konishi et al. 2008, 2010; Ferrari and Viti 2010). Several occurrences of triple-chain silicate in amphiboles from lithologies hosting magmatic-hydrothermal ore deposits, e.g., the Atakani skarn, Japan (Akai 1982), Wirrda Well IOCG deposit, South Australia (Ciobanu et al. 2022) and metamorphosed nickel ores from the Norseman-Wiluna belt, Western Australia (Akai et al. 1997) are still related to the presence of mafic/ultramafic rocks.

A notable exception is the unusual occurrence of ‘wide chain Ca-pyriboles’ precipitated under a geothermal gradient within sediment-hosted cavities from the Salton Sea Geothermal Field, California (Yau et al. 1986). In this case, primary growth at greenschist facies conditions (~300 °C; 1 to 1.5 km) is considered, based on the NCP-pyribole associations and their micro- to nanoscale textures. Likewise, calcic-rich analogues of clinojimthompsonite are reported from Oeyama ophiolite, Japan (Konishi et al. 1993) that compare with the NCPs-rich, calcic amphiboles reported here (Fig. 2d). The Fe-rich NCP varieties reported from the Norseman-Wiluna belt by Akai et al. (1997) are also represented in the NCPs intergrowths reported here (Fig. 4c).

An outstanding, novel feature of the Jatobá amphibole inclusions is the rhythmic Ca-Fe zonation, with bands ranging in width from tens or hundreds of nm (Figs. 3g, 5a) down to just a few nm (Fig. 9b), along the *a* direction. This type of zonation reinforces the idea of self-patterning via oscillatory chemical gradients in a closed, close-to-equilibrium system, i.e., a decoupling of inclusion growth from the enclosing magnetite. However, the silicate chain sequence remains unchanged throughout the zoning along *a* (e.g., Fig. 8a-d) contrasting with the self-patterning along *b* that can be attributed to formation of rhythmic polysome sequences (Fig. 10a, b). Hence, we suggest significant differences in growth kinetics during inclusion crystallization (faster along *a* compared to *b*). Taken together, these chemical-structural characteristics strengthen the idea of primary NCP crystallization during amphibole formation in magnetite.

In contrast to the above, the observed transition from NCP-rich cummingtonite to Ce-bearing magnesio-hornblende along the *a* direction in a single inclusion (Figs. 5a, 9f) implies changes in the fluid signature from a mafic- to felsic-affiliation if we consider, for example, the REE enrichment in sodic amphiboles formed during the magmatic-hydrothermal evolution of peralkaline granitoids (Bernard et al. 2020). The Ce-concentration reported here (~6.7 wt.% Ce_2O_3) is however orders of magnitude higher than the tens to hundreds of ppm ΣREE measured in Na-amphiboles from six alkaline igneous complexes (Bernard et al. 2020). Such extreme REE concentrations can be attributed to the onset of the Jatobá magmatic-hydrothermal system with REE-rich fluids percolating through existing lithologies. Abundant Ce-bearing nanoparticles (Fig. 4a) are formed in magnetite adjacent to the orebody. Crystallization of thinner, Ce-bearing calcic amphibole inclusions is predominant and partially replaces pre-existing NCP-rich amphibole. Higher influx of percolating fluids is also recorded by the replacement of larger NCP-bearing aggregates by sheet silicates, dominantly talc (Fig. 14a). Moreover, these fluids are K- and Al-

bearing as indicated by formation of mica and/or chlorite (Fig. 14b, d-f). An increase in Al at this stage is also supported by the composition of Ce-bearing magnesio-hornblende from the same sample.

The highest Al contents are measured in Fts inclusions from the ore sample (Fig. 5b). Using Al^{tot} values of 2.47 and 2.59 a.p.f.u for the two Fts grains (Online Materials Table 1; Fig. 2d) and the formula $P(kbar)= 0.5 + 0.331(8) \times Al^{tot} + 0.995(4) \times (Al^{tot})^2$ for the revised Al-in-hornblende geobarometer (Mutch et al. 2016), we obtain pressures of 7.4 and 8.04 kbar. Such high-pressure might be attributed to shearing along faults during ore deposition. At this stage, magnetite has recrystallized resulting in most of the amphibole inclusions being lost (Fig. 1c). Some NCP-rich aggregates are nonetheless preserved, likely inherited from pre-ore stages. These display no marginal replacement by sheet silicates (Fig. 3c, and Online Materials Fig. A1).

Genetic implications

The evolution of magnetite, host to the amphibole-NCPs inclusions, is shown schematically in Figure 15. The earliest stage of magnetite formation is recorded by the NCP-amphibole inclusions preserved within mottled cores with irregular shapes. The morphology of the Mg-Fe-amphiboles (coarser aggregates, rounded shapes), the lack of coherence between the NCPs and host magnetite and the abundance of NCPs indicates formation during regional metamorphism of host lithologies and prior to the introduction of sulfides (Fig. 15a). Syn-metamorphic deformation is recorded by widespread chain-width disorder in NCPs. The second generation of inclusions, defined by their occurrence in thinner, euhedral amphiboles and the presence of zipper NCPs only marks an overprint of the core magnetite (Fig. 15b). At this stage, epitaxial growth of inclusions indicates magnetite recrystallization, which is also associated with a marked chemical change from Mg-Fe- to calcic, REE-bearing amphibole (actinolite; Ce-bearing Mg-hornblende). Such minerals,

together with their REE-enriched signature are typical of deposition from magma-derived hydrothermal fluids during the onset of IOCG systems (Corriveau et al. 2016; Ciobanu et al. 2019; Courtney-Davies et al. 2020; Verdugo-Ihl et al. 2020).

The Jatobá orebodies are hosted along shear zones (Veloso et al. 2020) which act as channels focusing fluid flow resulting in obliteration of the mottled cores within magnetite (Fig, 15c). High pressure (~7.5 kbar) ferrotschemakite typifies the last generation of amphiboles, which is associated with formation of biotite+titanite. Despite this reworking, the magnetite still preserves NCP-rich Mg-Fe-amphiboles from the earliest stage.

Although only very few amphiboles were observed in the studied mafic/ultramafic sample, the amphibole species described in magnetite have been recorded among the many varieties reported from host diabase and ore-associated magnetite at Jatobá (Veloso et al. 2020). The paragenetic scheme developed by Veloso et al. (2020) differs, however, from our interpretation in that they considered the multiple generations of calcic and Mg-Fe amphiboles to have formed through the deposit evolution, from pre- to ore-stages.

This is the second reported occurrence of a NCPs-amphibole association in magnetite from an IOCG system. However, in contrast to that documented from Wirrda Well, South Australia (Ciobanu et al. 2022), the Jatobá magnetite does not show silician defects. This difference may be attributed to the longer history of magnetite overprinting at Jatobá causing obliteration of such features. The discovery of NCPs in amphiboles represents a strong link between magnetite from the Neoarchean Carajás Province (Brazil) and the Mesoproterozoic Olympic Province, South Australia, the two largest IOCG terranes on Earth.

SUMMARY AND IMPLICATIONS

Results of this work are summarized as follows:

1. Jatobá magnetite hosts monoclinic amphiboles and NCPs within mottled cores or as sparse inclusions along {111} directions. The NCPs and amphiboles form polysomatic intergrowths along the *b* axis documented using HAADF STEM imaging on [001] zone axis. This is the first occurrence of clinojimthompsonite within magnetite and our observations represent one of the widest ranges of chain silicates yet recorded, up to 15-I_{beam} chains. Single to triple rows of I_{beam} zippers, including pyroxene slabs, in amphibole are the simplest intergrowths.

2. EDS STEM mapping shows two chemical populations: Mg-Fe- and Ca-(Al)-amphiboles, dominantly cummingtonite and actinolite; the first category being richer in NCPs. The calcic amphiboles include Ce-rich (up to 6.7 wt.% Ce_2O_3) varieties of Mg-hornblende and (ferro)tschermakite, with the compositions $^{B}(Ca_{1.66}v_{0.34})_2{}^{C}(Mg_{2.37}Fe^{2+}_{1.11}Al_{0.64}Fe^{3+}_{0.53}Ce_{0.36})_5{}^{T}(Si_{7.16}Al_{0.84})_8O_{22}(OH)_2$, and $^{A}(Ca_{0.43}Na_{0.27}K_{0.13}v_{0.17})_1{}^{B}(Mg_{0.44}Ca_{1.56})_2{}^{C}(Fe^{2+}_{1.94}Mg_{1.45}Al_{0.9}Fe^{3+}_{0.7}Ti_{0.02})_5{}^{T}(Si_{6.37}Al_{1.64})_8O_{22}(OH)_2$, respectively.

3. Based on HAADF STEM imaging, we formulate a relationship between the increase in the number of *C* and *A* cations from amphibole (2-I_{beam}) to n chain silicates (nI_{beam}) as: $nI_{beam} = T(2+n) = C(5+3n) = A(1+n)$, n=integer. The increase in the number of *C* and *T* cations controls expansion of the *b* unit cell parameter (by ~9 Å per additional I_{beam}). The *a* and *c* parameters remain relatively constant. Using this formula, we produced empirical models of crystal structures for 4- and 5-I_{beam} chain silicates. These models were validated by STEM simulation.

4. Although no discrete polysomes could be defined, the NCP-amphibole intergrowths have I_{beam} averages ($\bar{I}_{beam}$) around 2.5-2.7 (composition between Mg-Fe amphiboles and clinojimthompsonite).

5. Co-crystallization of double- and triple-chain silicate structures in many cases with rhythmic intergrowths as larger blocks along *b* is often accompanied by rhythmic Ca-Fe zonation along *a*. Such chemical-structural characteristics strengthen the idea of primary NCP crystallization via self-patterning during amphibole growth in magnetite in a close-to-equilibrium system.

6. Chain-width disorder is documented from a wide range of defects, e.g., planar faults, derailments, jogs, swells, assisting changes of the intergrowth sequences. Many violations of zipper termination rules indicate primary growth rather than replacement. The latter is represented by sheet silicates, dominantly talc but also biotite and chlorite, which replace coarser NCP-amphibole aggregates.

7. The multi-stage evolution of Jatobá magnetite is constrained from the amphibole-NCPs inclusions. The NCPs formed in abundance during the first cycle of magnetite growth (Mg-rich NCPs, talc present) within an [older] mafic/ultramafic lithology recording syn-shearing events (oblique defects, jogs, etc.). This was followed by formation of NCP-zippers in calcic-amphiboles and formation of some Ce-bearing species indicating fluid influx with IOCG signature at the onset of the mineralizing system. High-pressure Fts (~7.5 kbar) is formed in magnetite during shearing events associated with main ore deposition. NCPs are preserved throughout the history of magnetite overprinting.

This study shows the suitability of HAADF STEM imaging for depicting crystal structure modularity in pyriboles and NCPs since the images are readily interpretable in accordance with crystal structure models. The generic formula suggested here for chain silicates expansion towards longer I_{beam} numbers predicts new structures that need to be assessed in terms of their

thermodynamic stability. Discovery of Ce-rich amphibole offers an opportunity for research that can lead to models of REE incorporation into, and subsequent release from chain silicates.

The multi-stage amphibole-NCPs generations depicted here reinforce the idea that magnetite is a key mineral for tracking overprinting events in terranes with protracted geological histories. The study emphasizes the need for characterization down to the nanoscale when dealing with trace element concentrations and their distributions within a host mineral, in this case magnetite. All too commonly, genetic models and trace element substitution mechanisms are proposed based solely on empirical measurement of trace element concentrations without recognizing whether those elements are in solid solution or occur as nanoscale inclusions.

The occurrence of NCPs in magnetite from magmatic-hydrothermal deposits is likely to be widespread and is readily predictable in those deposits hosted by greenstone belts and other altered mafic/ultramafic complexes. Metamorphism and associated deformation, often obliterated in altered lithologies, can be tracked through careful observation of the range of micro-textures and/or defects in magnetite-hosted NCPs. On the other hand, the presence of key minerals (actinolite, biotite) and associated chemical signatures (K, Ca, REE) within magnetite provides clues to the early, alkali-calcic alteration stages in IOCG systems.

ACKNOWLEDGEMENTS AND FUNDING

We extend thanks to Animesh Bask for technical support with FIB analyses and Max Verdugo for his assistance with EDS analyses. Y.T.C.R and M.E.S acknowledges continuous support from the Brazilian Research Council (CNPq – Project 409015/2021-0) and the Coordenação de Aperfeiçoamento de Pessoal de Nível Superior - Brasil (CAPES) - Finance Code 001. Analytical expenses were supported by a grant from the Institute of Sustainability, Energy and Resources, The University of Adelaide. N.J.C. and K.E. acknowledge funding through Australian Research Council Linkage grant LP200100156 (Critical Minerals

from Complex Ores). We acknowledge constructive comments from two anonymous reviewers and thank Associate Editor Bradley De Gregorio for his handling of the manuscript.

REFERENCES

Akai, J. (1982) Polymerization process of biopyriboles in metasomatism at the Akatani ore deposit, Japan. Contributions to Mineralogy and Petrology, 80, 117-131.

Akai, J., Chiba, A., Konishi, H., Komatsu, M., and Matsubara, S. (1997) New occurrences of non-classical pyriboles formed during ocean-floor and regional metamorphism: estimated PT conditions of formation. European Journal of Mineralogy, 9, 1237-1255.

Ams, B.E., Jenkins, D.M., Boerio-Goates, J., Morcos, M.R., Navrotsky, A., and Bozhilov, K.N. (2009) Thermochemistry of a synthetic Na-Mg-rich triple-chain silicate: Determination of thermodynamic variables. American Mineralogist, 94, 1242-1254.

Bernard, C., Estrade, G., Salvi, S., Béziat, D., and Smith, M. (2020) Alkali pyroxenes and amphiboles: a window on rare earth elements and other high field strength elements behavior through the magmatic-hydrothermal transition of peralkaline granitic systems. Contributions to Mineralogy and Petrology, 175, 81.

Bozhilov, K.N. (2013) Structures and microstructures of non-classical pyriboles. EMU Notes in Mineralogy, 14, 109-152.

Bozhilov, K.N., Brownstein, D., and Jenkins, D.M. (2007) Biopyribole evolution during tremolite synthesis from dolomite and quartz in CO_2-H_2O fluid. American Mineralogist 92, 898–908.

Buseck, P.R., and Iijima, S. (1974) High resolution electron microscopy of silicates. American Mineralogist, 59, 1-21.

Campo-Rodríguez, Y.T., Schutesky, M.E., de Oliveira, C.G., and Whitehouse, M.J. (2022) Unveiling the polyphasic evolution of the Neoarchean IOCG Salobo deposit, Carajás Mineral Province, Brazil: Insights from magnetite trace elements and sulfur isotopes. Ore Geology Reviews, 140, 104572.

Ciobanu, C.L., Cook, N.J., Utsunomiya, S., Pring, A., and Green, L. (2011) Focussed ion beam–transmission electron microscopy applications in ore mineralogy: Bridging micro- and nanoscale observations: Ore Geology Reviews, 42, 6–31.

Ciobanu, C.L., Verdugo-Ihl, M.R., Slattery, A., Cook, N.J., Ehrig, K., Courtney-Davies, L., and Wade, B.P. (2019) Silician magnetite: Si–Fe-nanoprecipitates and other mineral inclusions in magnetite from the Olympic Dam Deposit, South Australia. Minerals, 9, 311.

Ciobanu, C.L., Verdugo-Ihl, M.R., Cook, N.J., Ehrig, K., Slattery, A., and Courtney-Davis, L. (2022) Ferro-tschermakite with polysomatic chain-width disorder identified in silician magnetite from Wirrda Well, South Australia: A HAADF STEM study. American Mineralogist, 107, 765-777.

Corriveau, L., Montreuil, J.F., and Potter, E.G. (2016) Alteration facies linkages among iron oxide copper-gold, iron oxide-apatite, and affiliated deposits in the Great Bear magmatic zone, Northwest Territories, Canada. Economic Geology, 111, 2045-2072.

Courtney-Davis, L., Ciobanu, C.L., Verdugo-Ihl, M.R., Cook, N.J., Ehrig, K.J., Wade, B.P., Zhu, Z.Y., and Kamenetsky, V.S. (2020) ~1760 Ma magnetite-bearing protoliths in the Olympic Dam deposit, South Australia: Implications for ore genesis and regional metallogeny. Ore Geology Reviews, 118, 103337.

Cressey, B.A., Whittaker, E.J.W., and Hutchison, J.L. (1982) Morphology and alteration of asbestiform grunerite and anthophyllite. Mineralogical Magazine, 46, 77-87.

Droop, G.T.R. (1994) Triple-chain pyriboles in Lewisian ultramafic rocks. Mineralogical Magazine, 58, 1-20.

Evans, B.W., and Yang. H. (1998) Fe-Mg order-disorder in tremolite-actinolite-ferro-actinolite at ambient and high temperature. American Mineralogist, 83, 458-475.

Ferrari, M., and Viti, C. (2010) Retrograde hydration sequence in disordered Mg amphiboles: A TEM investigation. American Mineralogist, 95, 81-91.

Grobéty, B.H. (1996) New short-range biopyribole polysomes from the Lepontine Alps, Switzerland. American Mineralogist, 81, 404-417.

Grobéty, B.H. (1997) The replacement of anthophyllite by jimthompsonite: a model for hydration reactions in biopyriboles. Contributions to Mineralogy and Petrology, 127, 237-247.

Hawthorne, F.C., Oberti, R., Harlow, G.E., Maresch, W.V., Martin, R.F., Schumacher, J.C., and Welch, M.D. (2012) Nomenclature of the amphibole supergroup. American Mineralogist, 97, 2031-2048.

Hatert, F., Mills, S.J., Pasero, M., Miyawaki, R., and Bosi, F. (2023) CNMNC guidelines for the nomenclature of polymorphs and polysomes. Mineralogical Magazine, 87, 225-232.

Huang, X.W., and Beaudoin, G. (2021) Nanoinclusions in zoned magnetite from the Sossego IOCG deposit, Carajás, Brazil: Implication for mineral zoning and magnetite origin discrimination. Ore Geology Reviews, 139, 104453.

Huang, X.W., Beaudoin, G., and Yang, Y. (2022) A HR-TEM study on two generations of magnetite from the Alemao IOCG deposit, Carajás, Brazil: Implication for Fe-Cu mineralization. Ore Geology Reviews, 146, 104934.

Jenkins, D.M., Gilleaudeau, G.J., Kawa, C., Dibiase, J.M., Fokin, M. (2012) Compositional limits and analogs of monoclinic triple-chain silicates. Contributions to Mineralogy and Petrology, 164, 229-244.

Konishi, H., Akai, J., and Kurokawa, K. (1993) Calcic analog of clinojimthompsonite from the Oeyama Ophiolite, Southwest Japan. Journal of the Geological Society of Japan, 99, 679-682.

Konishi, H., Buseck, P.R., Xu, H., and Li, X. (2008) Proto-polymorphs of jimthompsonite and chesterite in contact-metamorphosed serpentinites from Japan. American Mineralogist, 93, 351-359.

Konishi, H., Xu, H., and Dymek, R.F. (2010) High-resolution TEM study of jimthompsonite, chesterite, and chain-width disorder in Archean ultramafic rocks from Isua, West Greenland. American Mineralogist, 95, 73–80.

Leake, B.E., Woolley, A.R., ARPS, C.E.S., Birch, W.D., Gilbert, M.C., Grice, J.D., Hawthorne, F.C., Kato, A., Kisch, H.J., Krivovichev, V.G., and others. (1997) Nomenclature of amphiboles: report of the subcommittee on amphiboles of the international mineralogical association, commission on new minerals and mineral names. The Canadian Mineralogist, 35, 219-246.

Monteiro, L.V.S, Xavier, R.P., Hitzman, M.W., Juliani, C., de Souza Filho, C.R., and Carvalho, E. de R. (2008) Mineral chemistry of ore and hydrothermal alteration at the Sossego iron oxide–copper–gold deposit, Carajás Mineral Province, Brazil. Ore Geology Reviews, 34, 317-336.

Mutch, E.J.F., Blundy, J.D., Tattich, B.C., Cooper, F.J., and Brooker, R.A. (2016) An experimental study of amphibole stability in low-pressure granitic magmas and a revised Al-in-hornblende geobarometer. Contributions to Mineralogy and Petrology, 171, 85.

Najorka, J., and Gottschalk, M. (2003) Crystal chemistry of tremolite-tschermakite solid solutions. Physics and Chemistry of Minerals, 30, 108-124.

Nespolo, M., and Bouznari, K. (2018) Modularity of crystal structures: a unifying model for the biopyribole–palysepiole series. European Journal of Mineralogy, 29, 369-383.

Ridolfi, F., Zanetti, A., Renzulli, A., Perugini, D., Holtz, F., and Oberti, R. (2018) AMFORM, a new mass-based model for the calculation of the unit formula of amphiboles from electron microprobe analyses. American Mineralogist, 103, 1112-1125.

Schumacher, J.C., and Czank, M. (1987) Mineralogy of triple- and double-chain pyriboles from Orijärvi, southwest Finland. American Mineralogist, 72, 345-352.

Schutesky, M.E., and de Oliveira, C.G. (2020) From the roots to the roof: An integrated model for the Neoarchean Carajás IOCG System, Brazil. Ore Geology Reviews, 127, 103833.

Thompson, J.B. Jr. (1978) Biopyriboles and polysomatic series. American Mineralogist, 63, 239-249.

Thompson, R.M., and Downs, R.T. (2008) The crystal structure of diopside at pressure to 10 GPa. American Mineralogist, 93, 177-186.

Veblen, D.R., and Burnham, C.W. (1978a) New biopyriboles from Chester, Vermont: I. Descriptive mineralogy. American Mineralogist, 63, 1000-1009.

Veblen, D.R., and Burnham, C.W. (1978b) New biopyriboles from Chester, Vermont: II. The crystal chemistry of jimthompsonite, clinojimthompsonite, and chesterite, and the amphibole-mica reaction. American Mineralogist, 63, 1053-1073.

Veblen, D.R., and Buseck, P.R. (1979) Chain-width order and disorder in biopyriboles. American Mineralogist, 64, 687-700.

Veblen, D.R., and Buseck, P.R. (1980) Microstructures and reaction mechanisms in biopyriboles. American Mineralogist, 65, 599-623.

Veblen, D.R., and Buseck, P.R. (1981) Hydrous pyriboles and sheet silicates in pyroxenes and uralites: intergrowth microstructures and reaction mechanism. American Mineralogist, 66, 1107-1134.

Veblen, D.R. (1991) Polysomatism and polysomatic series: A review and applications. American Mineralogist, 76, 801-826.

Veloso, A.S.R., Monteiro, L.V.S., and Juliani, C. (2020) The link between hydrothermal nickel mineralization and an iron oxide-copper-gold (IOCG) system: Constraints based on mineral chemistry in the Jatobá deposit, Carajás Province. Ore Geology Reviews, 121, 103555.

Verdugo-Ihl, M.R., Ciobanu, C.L., Cook, N.J., Ehrig, K., and Courtney-Davis, L. (2020) Defining early stages of IOCG systems: evidence from iron oxides in the outer shell of the Olympic Dam deposit, South Australia. Mineralium Deposita, 55, 429-452.

Verdugo-Ihl, M.R., Ciobanu, C.L., Cook, N.J., Ehrig, K.J., Slattery, A., Courtney-Davies, L., and Dmitrijeva, M. (2021) Nanomineralogy of hydrothermal magnetite from Acropolis, South Australia: Genetic implications for iron-oxide copper gold mineralization. American Mineralogist, 106, 1273-1293.

Yau, Y.C., Peacor, D.R., and Essene, E.J. (1986) Occurrence of wide-chain Ca-pyriboles as primary crystals in the Salton Sea Geothermal Field, California, USA. Contributions to Mineralogy and Petrology, 94, 127-134.

Figure captions

Figure 1. Reflected light (**a-d**) and BSE images (**e, f**) showing representative magnetite textures and location of FIB cuts (F) for S/TEM sample preparation. (**a, b**) Magnetite from the analyzed ore sample and

altered mafic/ultramafic rock. Note that sulfides are predominantly chalcopyrite (Ccp) in (**a**) and pyrite (Py) in **(b)**. (**c, d**) Details of subhedral magnetite grains from areas circled in a and b, showing silicate, sulfide and other inclusions as labelled. Note marginal corrosion, porosity and fractures. (**e, f**) Details of areas (rectangles in c and d) selected for FIB-slicing across silicate inclusions. In (**e**) acicular inclusions along $\{111\}_{magnetite}$ are crossed by bands mottled with finer inclusions. In (**f**), the magnetite core displays concentric zoning and is densely mottled with inclusions. The core outline is partially irregular; coarser ilmenite (Ilm) and voids are present in the middle. Abbreviations: Ap–apatite; Bt–biotite, Chl–chlorite.

Figure 2. (a-c) HAADF-STEM images showing variation in size and shape of NCP-bearing amphiboles from the three foils: (**a**) coarser aggregates (A1-4), (**b**, **c**) subrounded and euhedral, prismatic grains. Note fine-rhythmic intergrowths between NCPs (darker) and amphibole (lighter) along the length and presence of Fe-rich bands (lighter) across the width of the grains. The italicized numbers in brackets represent the I_{beam} average for analyzed amphibole-NCP sequences. The numbers highlighted in yellow correspond to data plotted in (d). (**d**) Amphibole classification plots (after Leake et al. 1997) showing two compositional groups, calcic-(left) and Mg-Fe-amphibole (right) using data from Online Materials Tables 1 and 2. Numbers 1-4 correspond to aggregates in (**a**); 5, 6 are analyses collated from small grains (e.g., map in Fig. 4a); 7-9 amphibole grains from various maps (e.g., Fig. 5b), and Ce-amphibole from the map in Fig. 5a. The aggregates numbered 1-4 are further sub-divided into (i) entire mapped grain, and (ii) selected area (no NCPs). Abbreviations: Act–actinolite, Amp–amphibole, Cum–cummingtonite, Fact–Ferro-actinolite, Fts–Ferro-tschermakite, Gru–grunerite, Hbl–hornblende, Mg-Hbl–magnesio-hornblende, Ts–tschermakite, Ttn–titanite.

Figure 3. Low-resolution images illustrating amphibole-NCP intergrowths from (**a**) rounded, and (**b**) subhedral grains, and (**c**-**g**) aggregates (areas marked on Figure 2). Crystal of clinojimthompsonite with amphibole intergrowths (lighter bands) in (**a**). Note changes in chemical composition along and parallel to the intergrowths in (**c**, **g**) and (**d**, **f**) respectively. Profile in (**c**) shows the inverse variation between Mg, Ca (dark) and Fe (light) across banding. Crop in (**g**) shows that the same I_{beam} structures are preserved across

chemical banding with respect to Fe (lighter) and Ca (darker) (see map in Fig. 4c). Boundaries between distinct phases are marked by dashed lines. Abbreviations: Act–actinolite, Cum–cummingtonite, Tlc–talc.

Figure 4. STEM EDS maps and overlays of (**a**) densely mottled areas, (**b**) aggregate 3, and (**c**) aggregate 2. Inset in (**a**) shows Ce-rich nanoparticles attached to amphiboles. (**b**) Aggregate comprising NCP rich (NCP>) cummingtonite (Cum) and NCP poor (NCP<) actinolite (Act). Fine-rhythmic banding with respect to Fe across the NCP-rich cummingtonite from aggregate 2. Note straight contacts (dotted line) with marginal actinolite. The numbers highlighted in yellow correspond to data plotted in Figure 2d.

Figure 5. STEM EDS maps and overlays showing (**a**) Ce-bearing magnesio-hornblende (Ce-Mhbl), and (**b**) (ferro)-tschermakite (Fts). In (**a**), the top part corresponds to cummingtonite (Cum) displaying Ca-Fe rhythmic zonation. Note biotite (Bt) on the side of Fts in (**b**). The number highlighted in yellow corresponds to data plotted in Figure 2d.

Figure 6. Models and images of chain silicates as labelled, each plotted on [001] zone axis. The structures used for the three models at the top are: actinolite for amphibole (Evans and Yang 1998), clinojimthompsonite for triple-chain silicate, and chesterite for the alternating double and triple chain silicate (Veblen and Burnham 1978b). Empirical models for the 4- and 5-I_{beam} structures (bottom) are shown and compared with STEM simulations; these can be compared with images in Figure11d. I-beam outlines as overlays on atom-fill models. Note increase in the I_{beam} number is associated with increase in the length of *b* (by ~9 Å). Legend for cation positions is according to the general amphibole formula of Hawthorne et al. (2012): $AB_2C_5T_8O_{22}W_2$, where *A* = vacancy (□), Na, K, Ca, Pb, Li; *B* = Na, Ca, Mn^{2+}, Fe^{2+}, Mg, Li; *C* = Mg, Fe^{2+}, Mn^{2+}, Al, Fe^{3+}, Mn^{3+}, Ti^{4+}, Li; *T* = Si, Al, Ti^{4+}, Be; and *W* = (OH), F, Cl, O^{2-}. See text for further explanations.

Figure 7. HAADF STEM images (**a**, **b**, **e**), atom fill models and I-beam schematics (**c**, **d**) for pyroxene slabs as zippers in other chain silicates for [001] zone axis. Diopside structure used for pyroxene model (Thompson and Downs 2008). A single slab of pyroxene, parallel with (010), is shown within amphibole

in (**a**) and between amphibole and triple chain silicate in (**b**). (**c**, **d**) Overlays on crystal models show the I_{beam} for pyroxene. The joint between 1-I_{beam} with 2- and 3-I_{beam} structures is realised by *a*/2 offset of the pyroxene central ribbon relative to that in the host silicate. Adjacent ribbons in the host silicates are separated by gaps (red diamonds) smaller than the *A* site (grey diamond) which is not present in pyroxene. The I_{beam} schematics show the resulting polysomes, numbers underneath: (212) and (213), respectively. (**e**) Polysomatic sequence in amphibole showing four pyroxene slabs across an interval of ~20 nm, two of which are placed at contacts with 5-I_{beams}.

Figure 8. (**a**-**d**) Larger (up to 100 nm-long) polysomatic sequences from aggregates (A1-3) along profiles marked on Figure 3c, d, and g. The NCPs sequences within amphibole are marked by numbers in the blue boxes. Note compositional boundaries (dashed lines) in a, c and d. The average $\bar{I}_{beam}$ for these sequences is in the range 2.22-2.68. (**e**, **f**) I_{beam} schematics showing zipper terminations for areas as labelled by circled numbers. Coherent terminations are shown in (**e**). The red I_{beams} in (**f**) show derailment for case 5 and a zipper modification breaking termination rule 1.

Figure 9. High-resolution images of amphiboles showing chain-width disorder and chemical zoning. (**a**) Single and double zippers of 4-I_{beam} with modifications across a Fe-rich chemical band in the middle of the image. The grain displays pyroxene zippers and a more regular sequence of triple-chain silicate towards the boundary to magnetite. Inset shows the zipper termination (arrowed) breaking rule 2. (**b**) Narrow (<5 nm-wide) Fe-rich bands (brighter) along the *b* axis in a regular sequence of amphibole. (**c**, **d**) Fe-rich bands crossing single and triple zippers without changes in the structure. Inset in (**c**) shows fast Fourier transform (FFT) pattern on [001] actinolite (grain mapped in Figure 4c) obtained from the whole image. Note presence of $(\bar{1}10)$ reflections indicative of monoclinic symmetry. (**e**) Epitaxial contact between $[001]_{amphibole}$ and $[112]_{magnetite}$ typical for the zipper-bearing amphiboles. FFT pattern shows $(100)^*_{Amph}//(111)^*_{Mag}$. (**f**) Boundary between NCP-rich cummingtonite (top) and Ce-bearing magnesio-hornblende (bottom) (grain mapped in Figure 5a). FFT pattern in inset obtained from the bottom part shows this is a monoclinic

amphibole. (**g**, **h**) High-resolution images from areas marked on (**f**) showing the sequences in the two amphiboles. Note rare pyroxene and triple chain zippers in (**g**) and denser NCPs in (**h**).

Figure 10. (**a**, **b**) Wider, more regular blocks triple chain slabs (up to 23; in blue) within amphibole (grey ribbon underneath). Sequence in (**b**) represent a full transect of clinojimptomsonite (Cjim) (grain in Figure 3a) shown as high-resolution images in (**c**-**f**). FFT pattern as inset to (**c**) is from the whole image. (**d**) Regular sequence (>17 slabs) of Cjim. STEM simulation shown as overlay. (**e**, **f**) Polysomatic disorder as (523) and (235) sequences on the edges of sequence in (**c**).

Figure 11. High-resolution images showing polysomes with the widest I_{beams} and I_{beam} schematic. (**a**) Sequences comprising (737) and (45355656) polysomes in amphibole and triple-chain silicate. (**b**, **c**) Sequences with 11- and 12-I_{beam} structures with changes along *a* direction. (**d**) Details of NCPs with I_{beams} in the ranges 4-7 and 9, 11 and 12. Note the numbers of diamond-shaped motifs (A sites) and the dots along the cation ribbon (B+C sites) in agreement with formula (1). (**e**) Termination of 3- and 5-I_{beam} zippers breaking rule 1.

Figure 12. Overview of chain-width disorder and defects in NCP-rich amphiboles as images and I_{beam} schematics. (**a**) Field showing a wide range of defects as chain derailment (dotted line), jogs (white arrows) and hairpin structures (yellow arrows). Normal fault with displacement movement marked in red. (**b**) Inverse fault (movement marked in red) transforming zippers sequences (as numbered) in amphibole with violation of both termination rules. (**c**) Detail from (a) showing jog defect zipper transformation. (**d**) Oblique defects (arrowed) in the vicinity of 15-I_{beam} zipper with multiple width changes along *a*. (**e**) Occurrence of the 8-I_{beam} zipper along a 4-I_{beam} derailment in amphibole. (**f**) Detail from (d) showing formation of the 10-I_{beam} structure. (**g**, **h**) Neighbourhood of 8- and 10-I_{beams} structures showing changes in sequences breaking zipper termination rules.

Figure 13. Details of chain-width disorder and defects in NCP-rich areas as images and I_{beam} schematics. (**a**) *En-echelon* defects bridging 6-I_{beam} zippers via the (233535) polysome. (**b**) Coherent zipper termination

linking multiple NCP zippers. (**c**) Oblique defects marking a shear plane (arrowed) cutting across triple- and double-chain sequences with changes breaking termination rule 1. (**d**) Detail of jogs showing displacement along *b* assisting changes between 3- and 4-I_{beam} structures (note violation of rule 1). (**e**, **f**) Wide NCP zippers with single and double pull-apart swells shown as schematics in (**g**, **h**). Note violation of termination rule 2 in both cases. (**i**, **j**) Short, double terminations zipper with coherent and incoherent ends. (**k**) Arcuate defect assisting coherent zipper termination. (**l**) Schematic showing area from rectangle in (a) showing a switch between 6- and 5-I_{beams} breaking both termination rules.

Figure 14. Overview of replacement between sheet and chain silicates. (**a**) Contact between $[100]_{Tlc}$ and $[001]_{Cum}$. Note the ragged contact outline with ledges (arrowed) and voids (dark areas). FFT pattern for talc (Tlc) as inset. (**b**) Stepwise contact between actinolite (Act) and sheet silicates comprising talc and a package of mica. FFT pattern (inset) shows coherent orientation between the two silicates which share b* axes. (**c**) Replacement front between talc and cummingtonite (Cum) along two directions with straight contact (c_{Tlc} parallel to a_{Cum}). Wide NCP zippers show increase of I_{beam} numbers toward the contact to talc. Swell defects (arrowed) produced by intercalation of chlorite (Chl). (**d**) Edge of cummingtonite showing replacement by talc with straight and stepwise (dotted line) contacts. Note a chlorite package (dashed line) and disorder (arrowed) in talc. (**e**) Contact between mica (FFT pattern indexed as biotite, Bt) and actinolite. (**f**) Chlorite (FFT pattern as inset) displaying stacking disorder intervals (marked) at the contact to talc (STEM simulation as overlay). (**g**) Swell defects (arrowed) in sheet silicates with mix packages (Tlc and Chl). (**h-j**) Models showing typical *T*-*O*-*T* packages (*T*, O=tetrahedral, octahedral layer) for the three sheet silicates. The packages are sandwiched with either K or *O* layers in biotite and chlorite. Note match between models and images above.

Figure 15. Schematic showing staged evolution of magnetite as labelled. (**a**) Metamorphic segregation results in lenses of magnetite with cores clustered by Mg-(Fe)-amphiboles with NCPs. (**b**) Recrystallized magnetite preserves cores mottled by new-formed Ca-(Ce)-amphiboles. NCPs-rich-amphiboles are preserved as rounded grains and aggregates with marginal replacement by sheet silicates. (**c**) Shearing and

brecciation of magnetite during ore stage accompanied by formation of high-pressure calcic-Al-amphiboles and mica. NCP-aggregates preserved from the first stage.

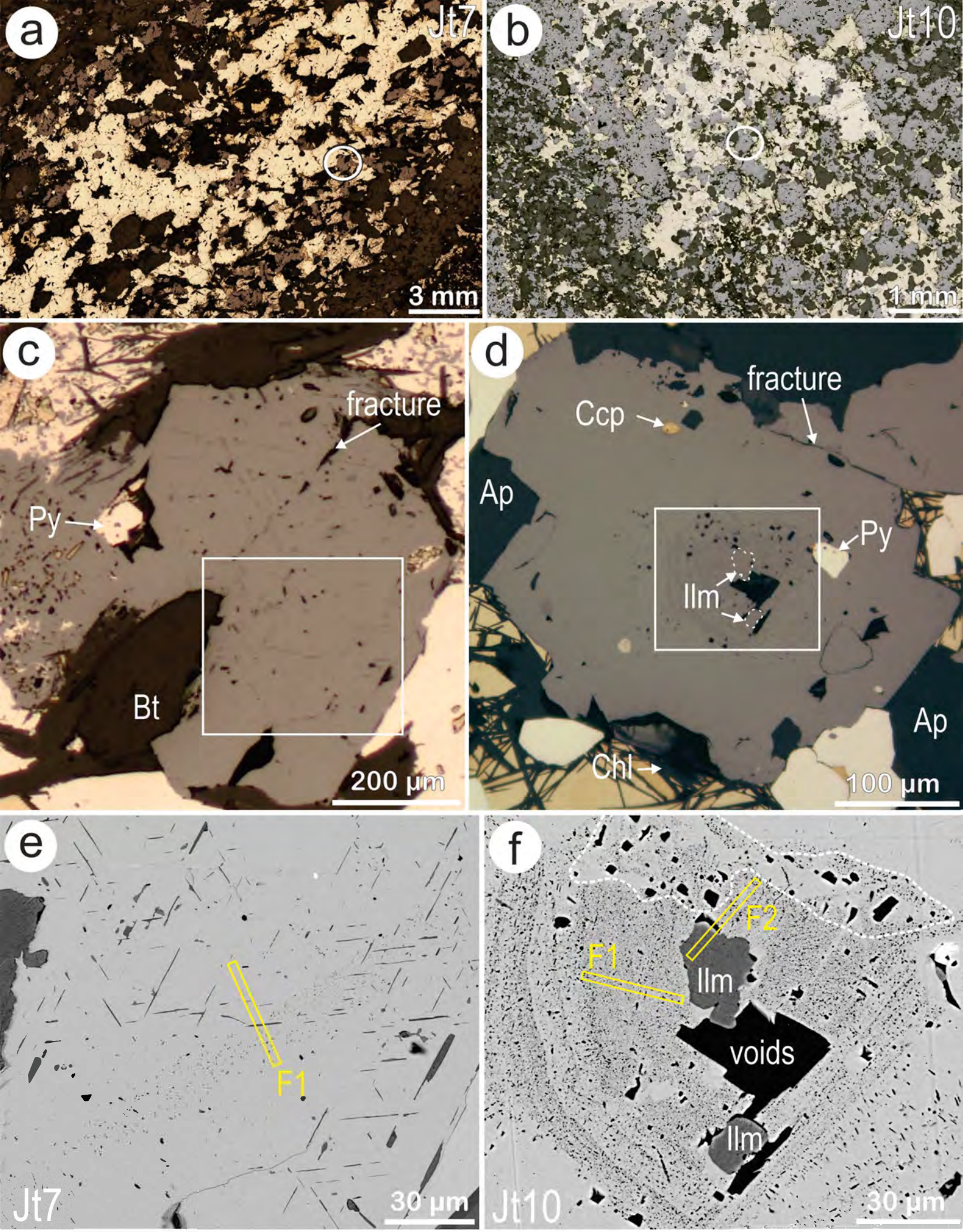

Figure 1. Campo-Rodriguez et al.

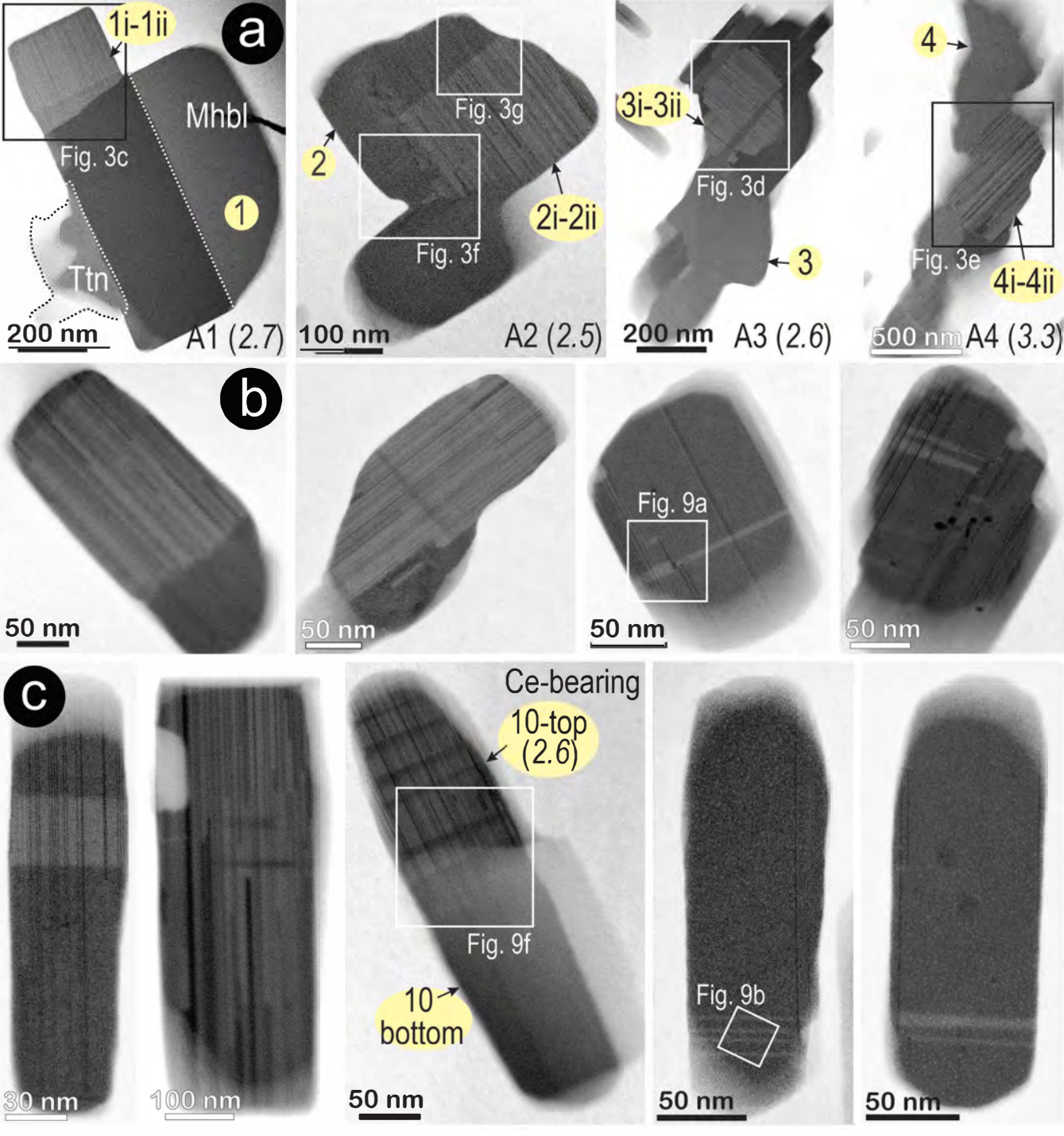

Figure 2. Campo-Rodriguez et al.

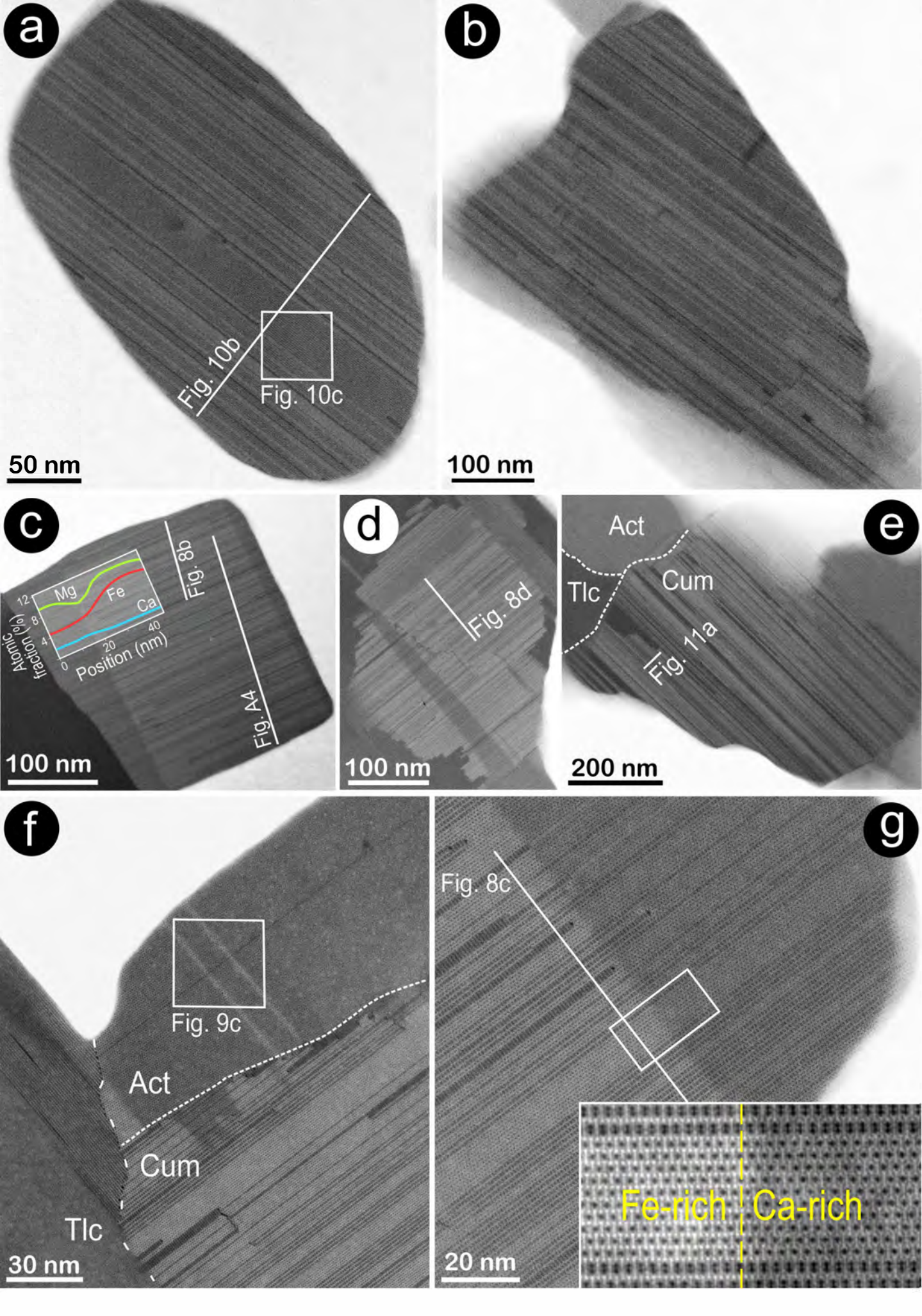

Figure 3. Campo-Rodriguez et al.

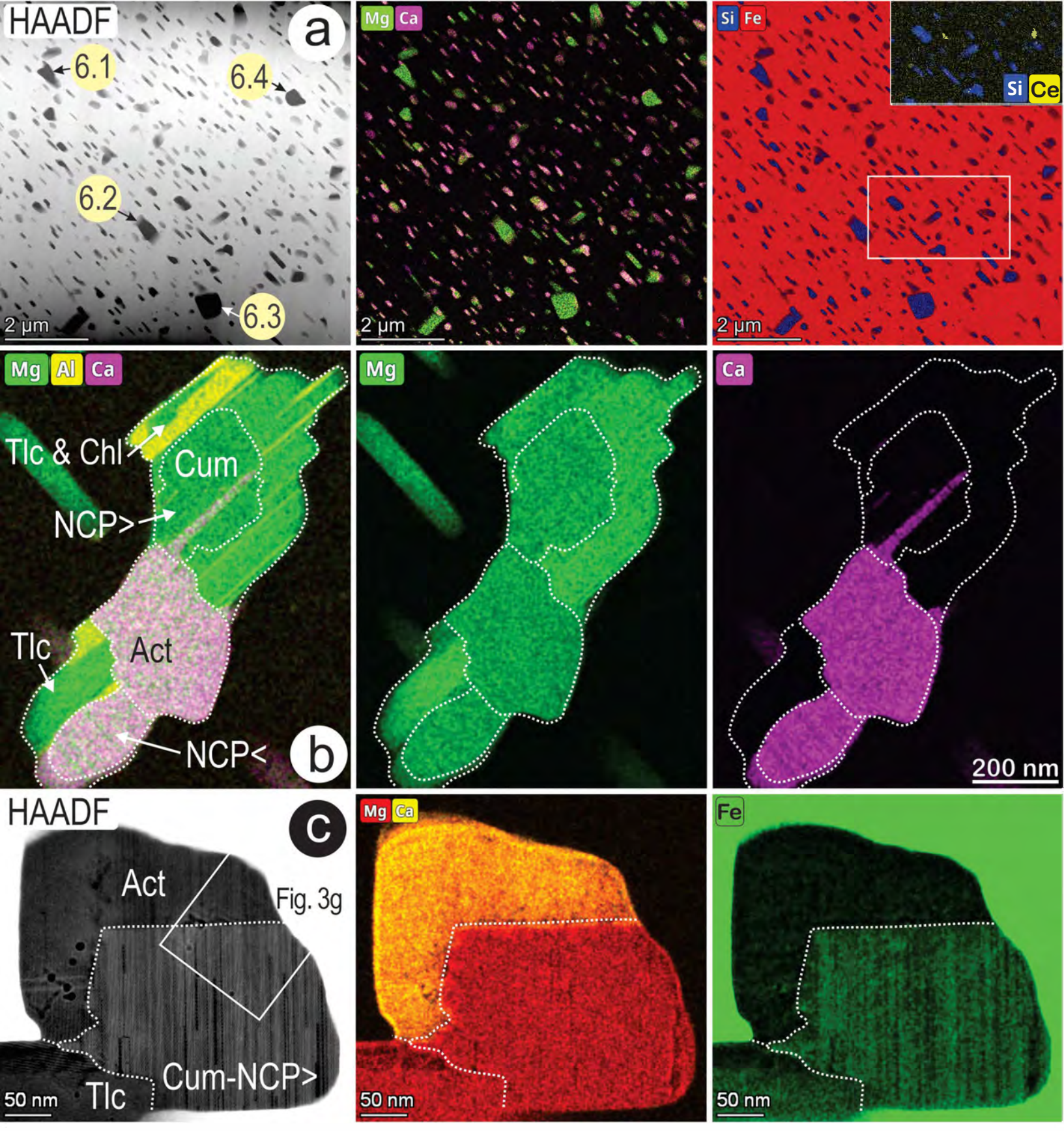

Figure 4. Campo-Rodriguez et al.

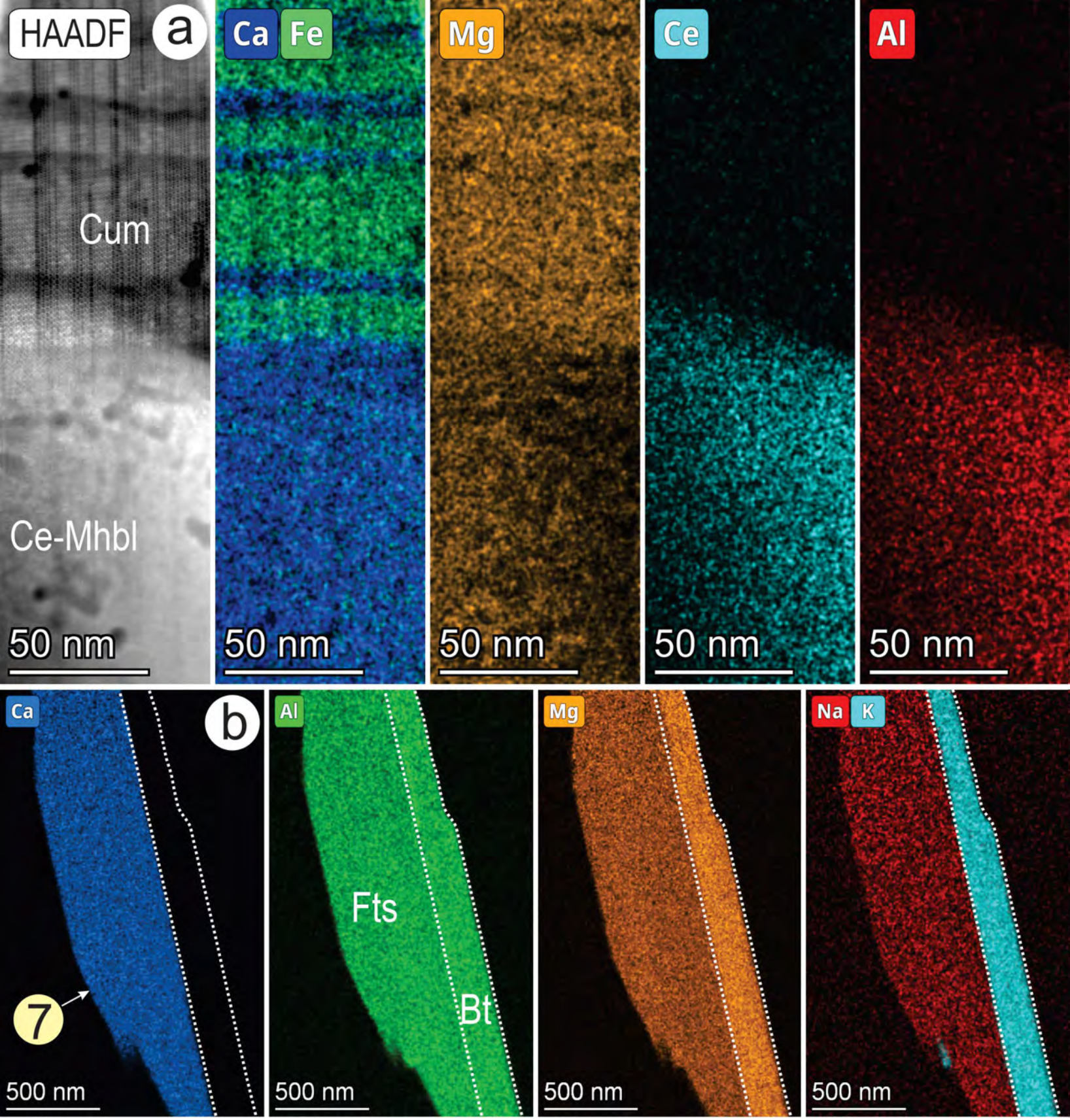

Figure 5. Campo-Rodriguez et al.

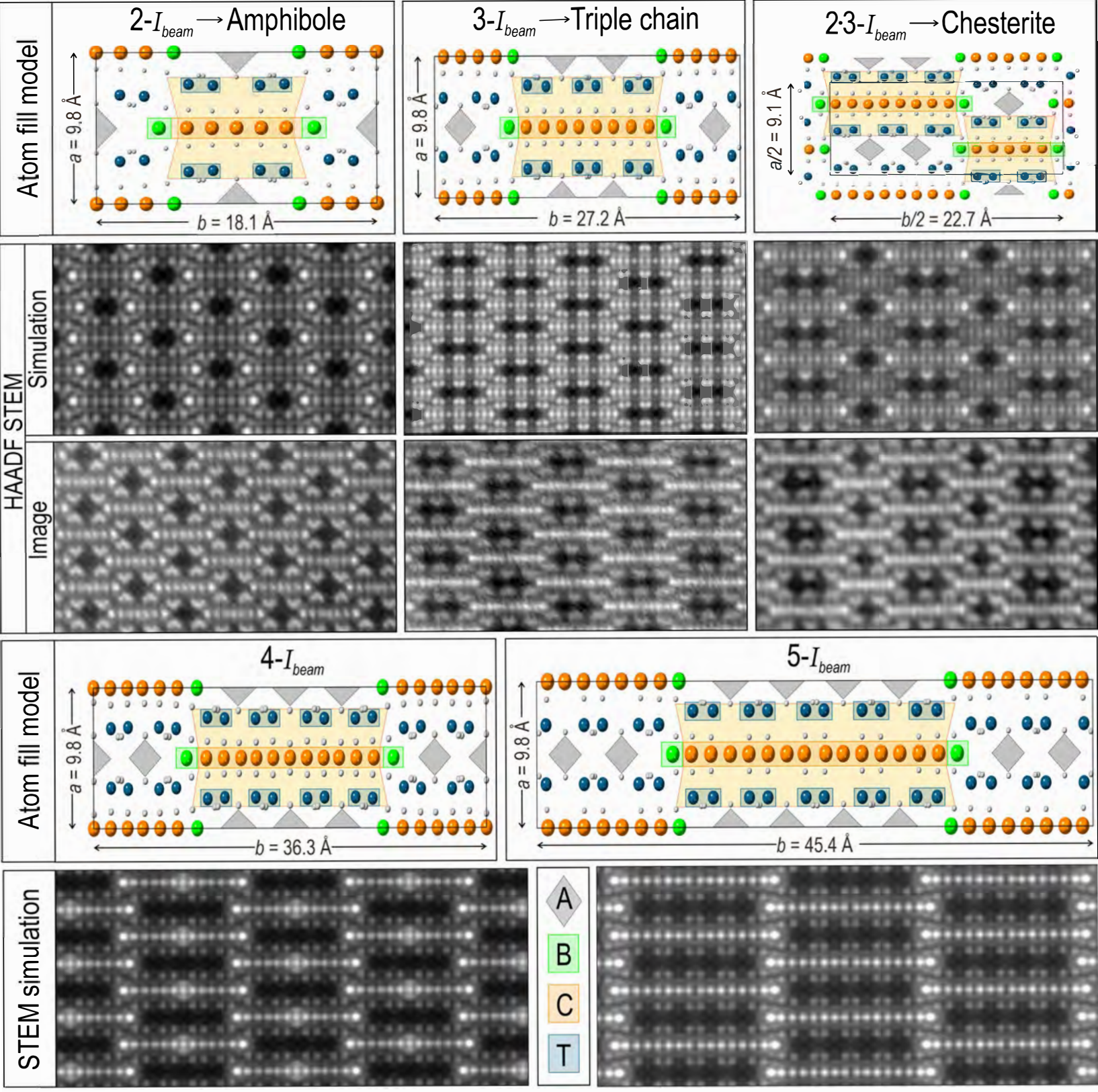

Figure 6. Campo-Rodriguez et al.

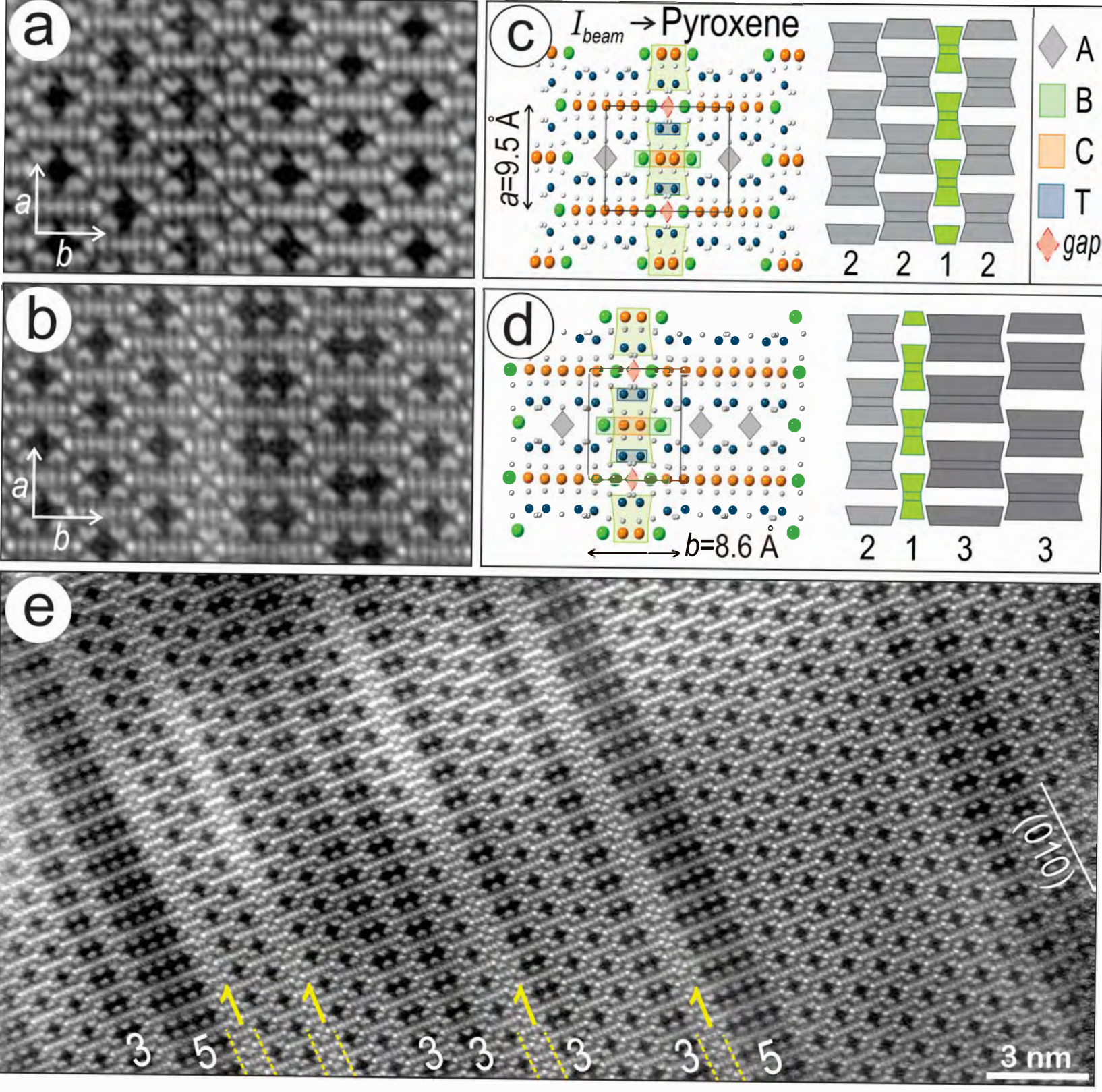

Figure 7. Campo-Rodriguez et al.

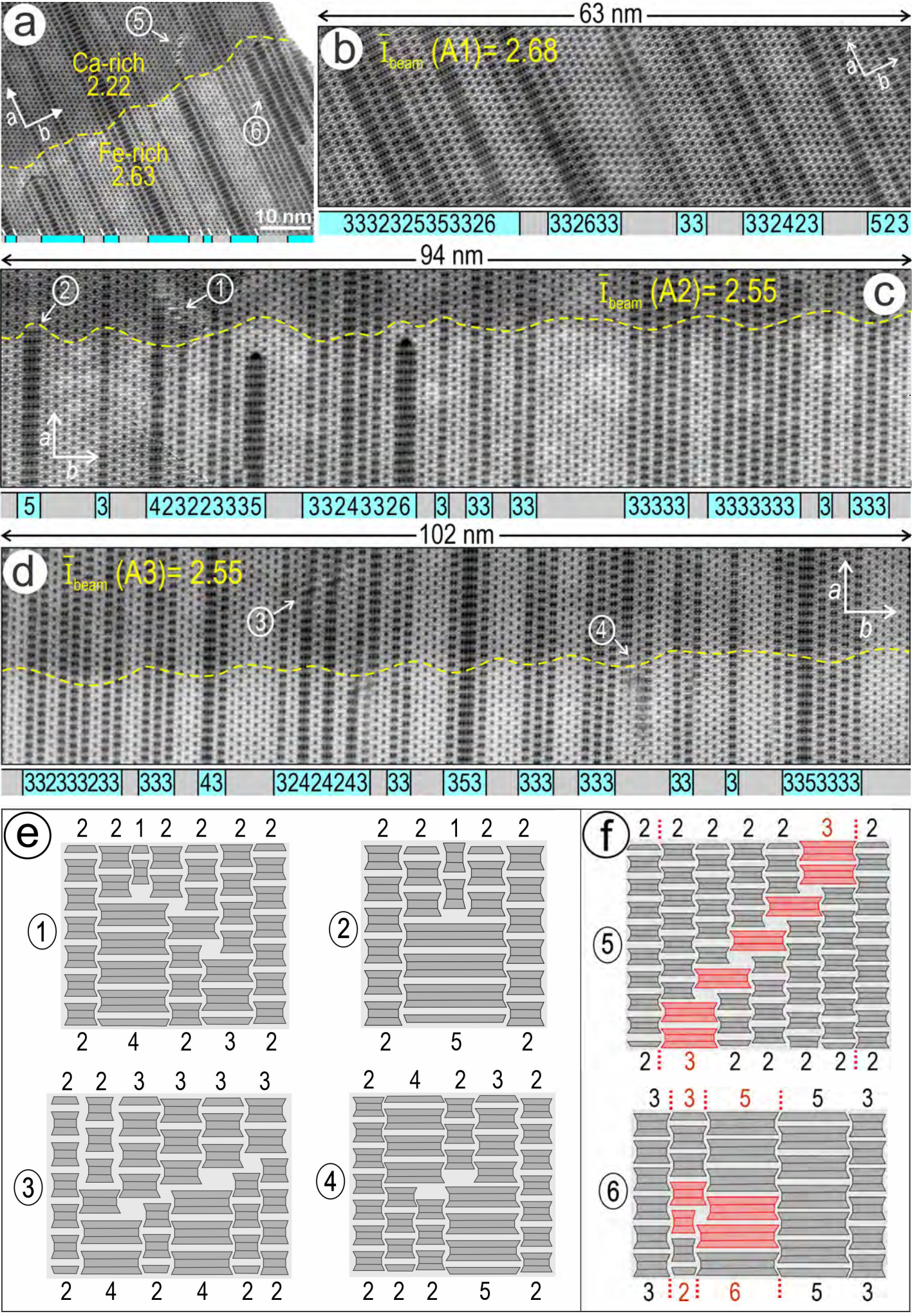

Figure 8. Campo-Rodriguez et al.

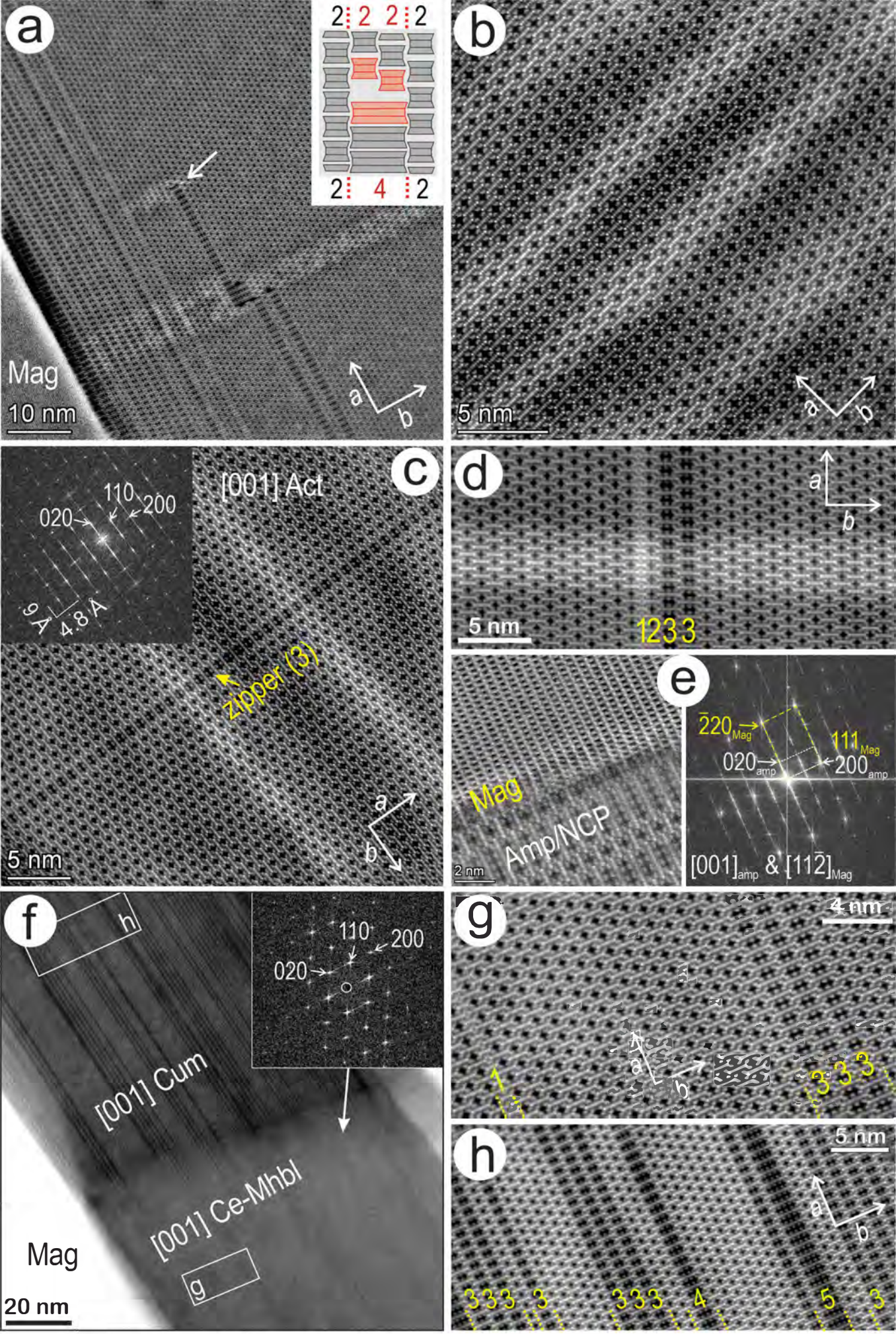

Figure 9. Campo-Rodriguez et al.

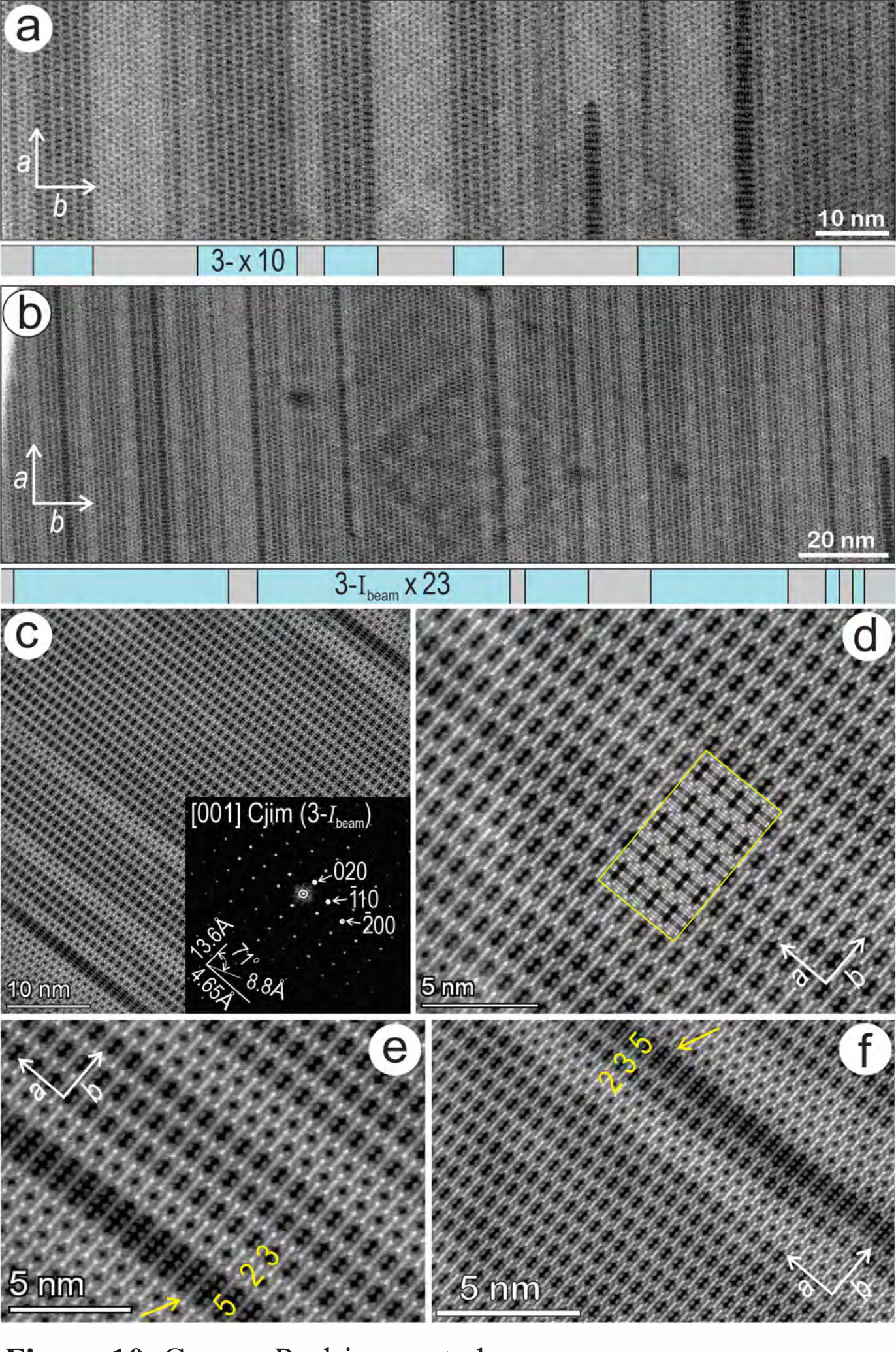

Figure 10. Campo-Rodriguez et al.

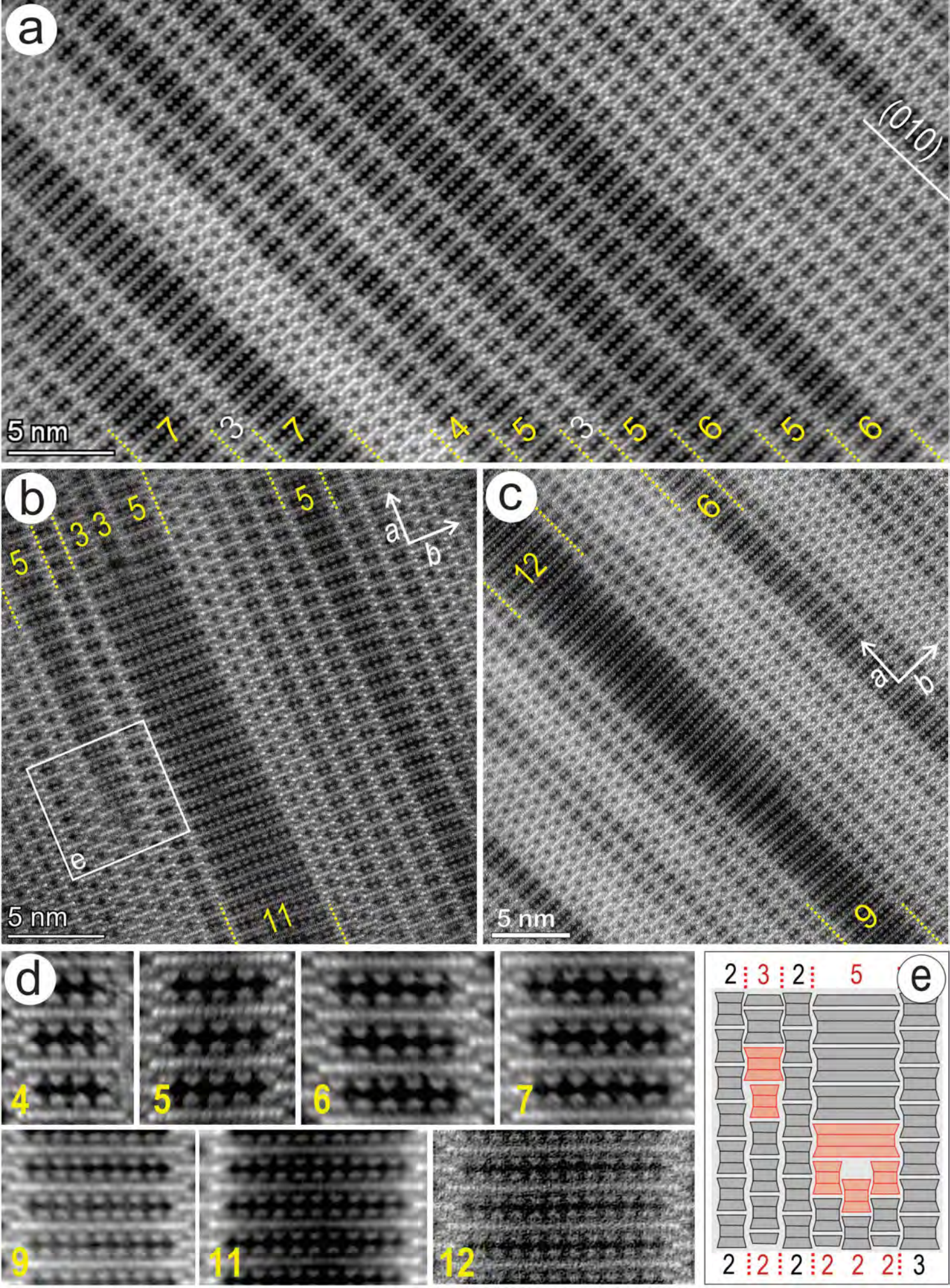

Figure 11. Campo-Rodriguez et al.

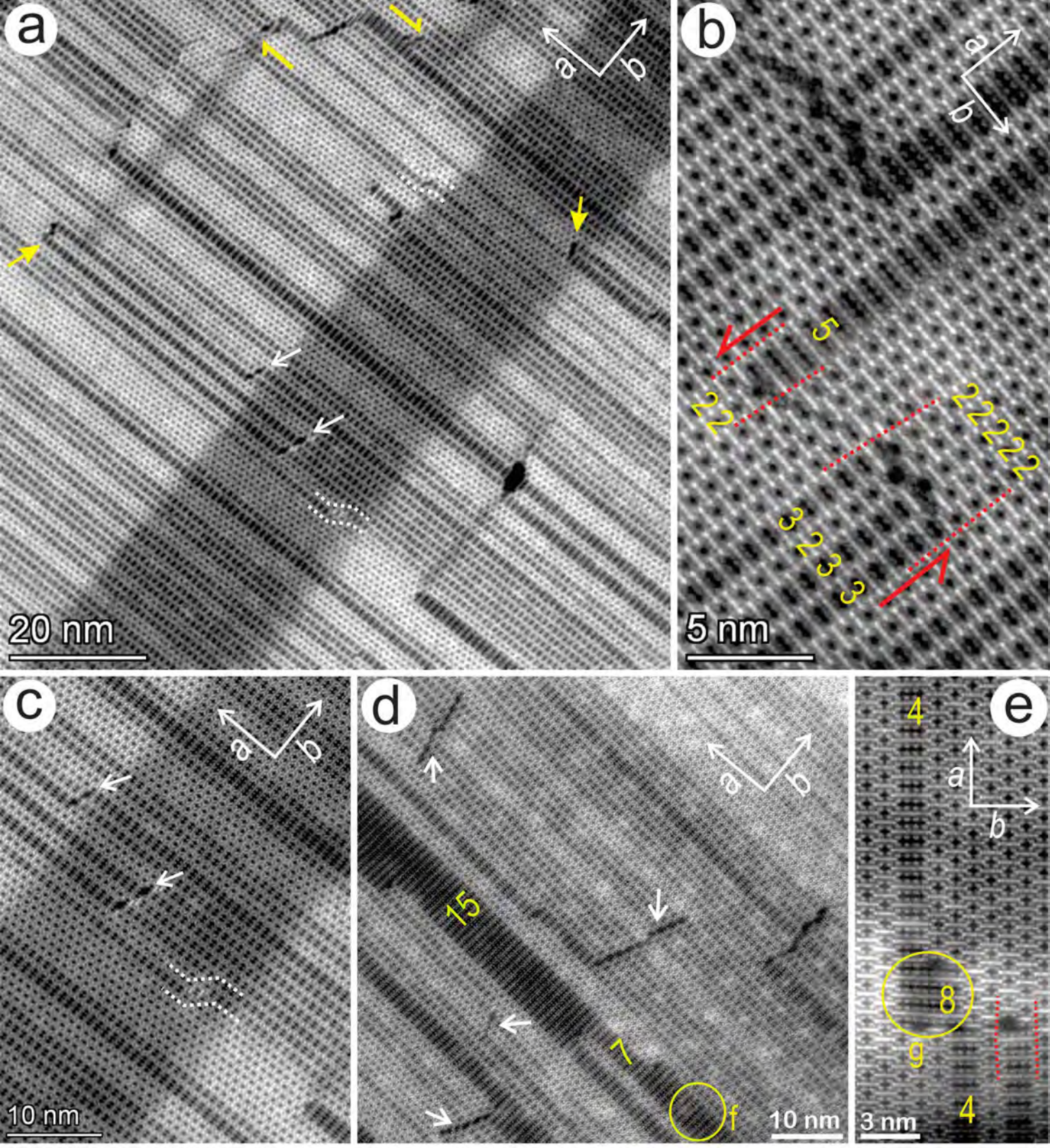

Figure 12. Campo-Rodriguez et al.

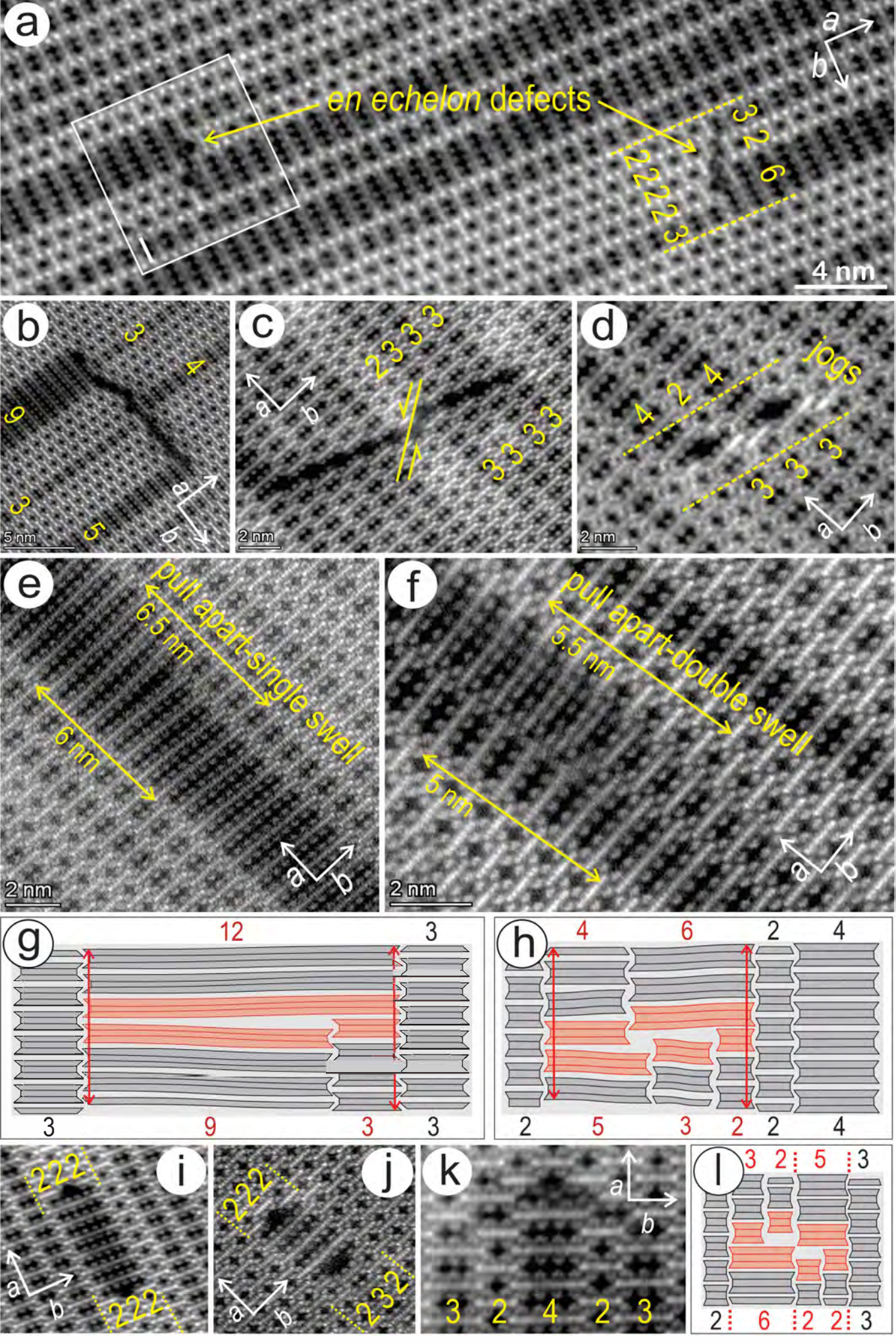

Figure 13. Campo-Rodriguez et al.

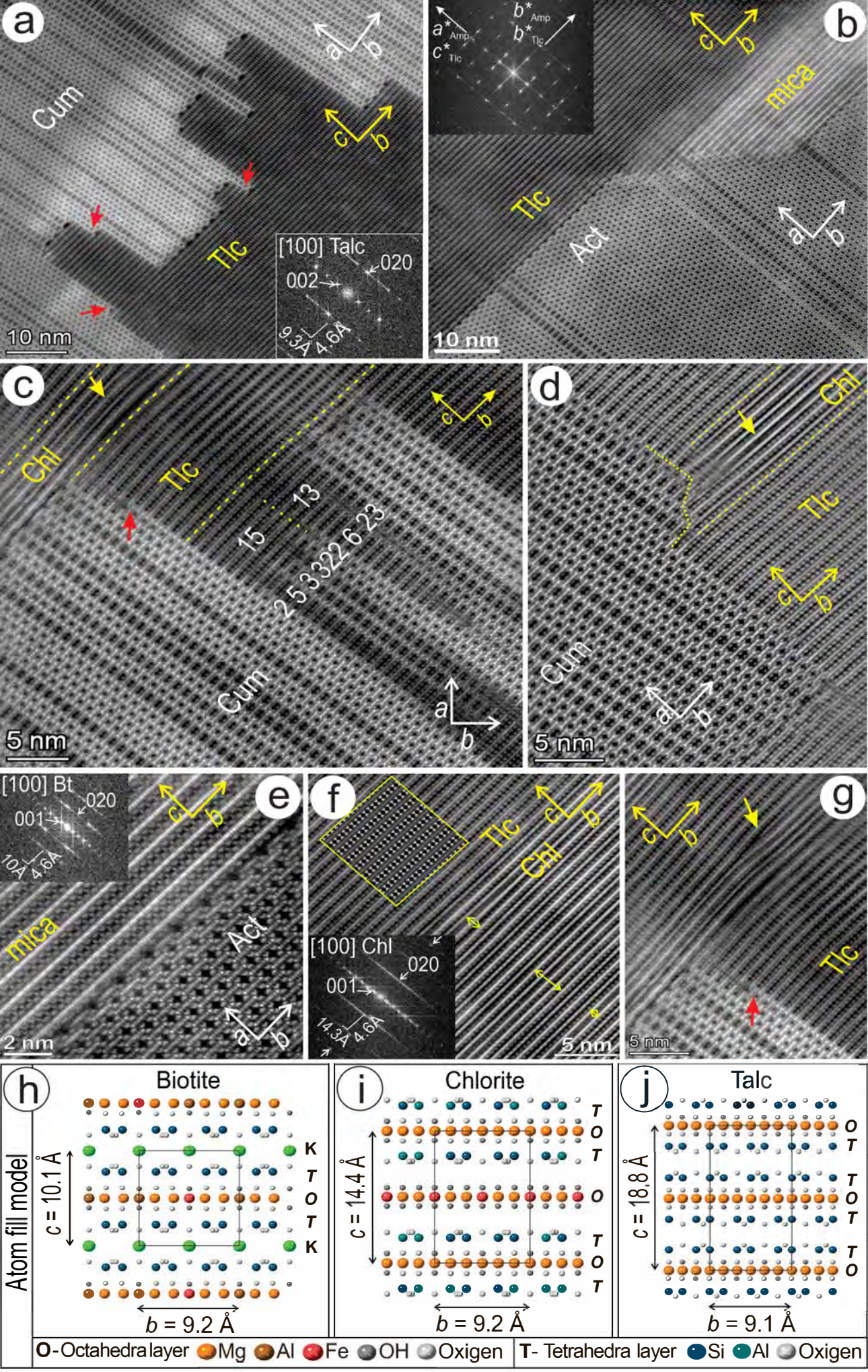

Figure 14. Campo-Rodriguez et al.

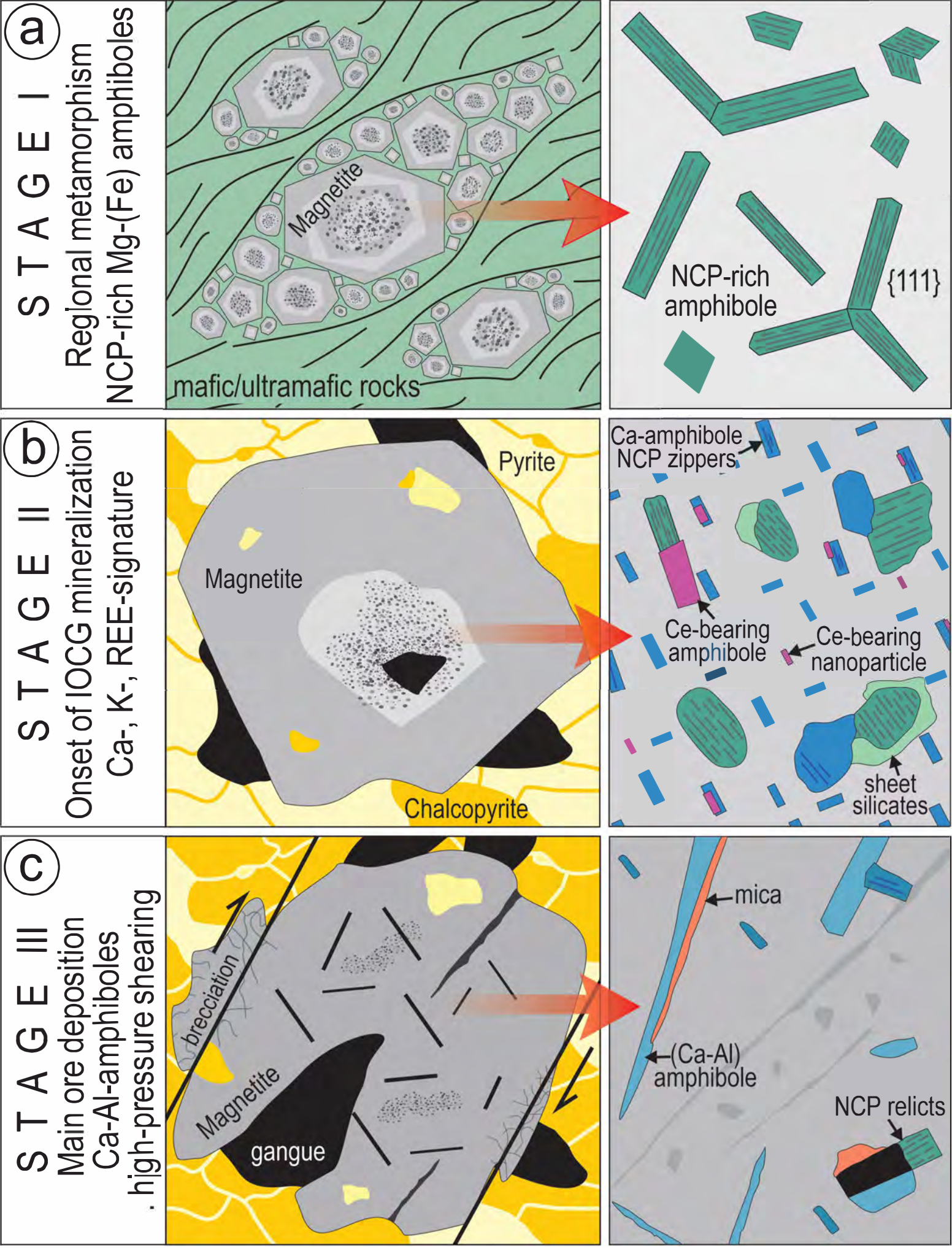

Figure 15. Campo-Rodriguez et al.